CHAPTER 5
CHEMICAL ENVIRONMENTS OF SUBMARINE HYDROTHERMAL SYSTEMS

EVERETT L. SHOCK

Department Earth and Planetary Sciences and McDonnell Center for the Space Sciences,

Washington University, St. Louis, MO, 63130 U.S.A.

1. Hydrothermal Systems vs. Hydrothermal Vents

Perhaps because black-smoker chimneys make tremendous subjects for magazine covers, the proposal that submarine hydrothermal systems were involved in the origin of life has caused many investigators to focus on the eye-catching hydrothermal vents. In much the same way that tourists rush to watch the spectacular eruptions of Old Faithful geyser with little regard for the hydrology of the Yellowstone basin, attention is focused on the spectacular, high-temperature hydrothermal vents to the near exclusion of the enormous underlying hydrothermal systems. Nevertheless, the magnitude and complexity of geologic structures, heat flow, and hydrologic parameters which characterize the geyser basins at Yellowstone also characterize submarine hydrothermal systems. However, in the submarine systems the scale can be considerably more vast. Like Old Faithful, submarine hydrothermal vents have a spectacular quality, but they are only one fascinating aspect of enormous geologic systems operating at seafloor spreading centers throughout all of the ocean basins. A critical study of the possible role of hydrothermal processes in the origin of life should include the full spectrum of probable environments.

The goals of this chapter are to synthesize diverse information about the inorganic geochemistry of submarine hydrothermal systems, assemble a description of the fundamental physical and chemical attributes of these systems, and consider the implications of high-temperature, fluid-driven processes for organic synthesis. Information about submarine hydrothermal systems comes from many directions. Measurements made directly on venting fluids provide useful, but remarkably limited, clues about processes operating at depth. The oceanic crust has been drilled to ~ 2.0 km depth providing many other pieces of information, but drilling technology has not allowed the bore holes and core samples to reach the maximum depths to which aqueous fluids circulate in oceanic crust. Such determinations rely on studies of pieces of deep oceanic crust uplifted by tectonic forces such as along the Southwest Indian Ridge, or more complete sections of oceanic crust called ophiolite sequences which are presently exposed on continents owing to tectonic emplacement. Much of what is thought to happen in submarine hydrothermal systems is inferred from studies of ophiolite sequences, and especially from the better-exposed ophi-

olites in Oman, Cyprus and North America. The focus of much that follows is on a few general features: pressure, temperature, oxidation states, fluid composition and mineral alteration, because these features will control whether organic synthesis can occur in hydrothermal systems.

2. The Formation of Ocean Crust and Submarine Hydrothermal Systems

The presence of hydrothermal systems at mid-ocean ridges is a consequence of the injection of magma and its subsequent solidification and cooling. Understanding the variation and extent of submarine hydrothermal systems requires an understanding of the origin and structure of the oceanic crust. The hypothetical cross-section of one side of an active spreading center on an oceanic ridge in Fig. 1 helps to emphasize the scale of submarine hydrothermal systems. Note that the horizontal axis is compressed somewhat relative to the vertical. New oceanic crust is generated at the spreading axis which overlies a magma chamber at the divergent plate boundary. Magma erupts from the chamber at depth through a system of feeder channels to the seafloor. The basalt which erupts at the crust/seawater interface is rapidly cooled by the overlying seawater. The outer shell of the liquid basalt hardens into a glassy rind, and tends to form small mounds or 'pillows' as it is quenched. Underlying the zone of pillow basalts is a transition zone of a few hundred meters which is underlain by vertical dikes. These dikes are the solidified predecessors of the active feeder channels at the spreading center. Basalt from previous eruptions fills these older dikes which extend symmetrically away from the spreading center. Underlying the sheeted dikes are the layered gabbros which are thought to represent the solidified analogues of the magma chamber. New pillow basalts and sheeted dikes are constantly formed at the spreading center and new gabbros form at the margins of the magma chamber. It follows that the age of the crust increases away from the spreading center as indicated by the scale at the top of the diagram.

Even on a human time scale fluids exit quickly from black-smoker vents, where flow rates up to 10 l sec^{-1} are common (Hekinian *et al.*, 1983; Converse *et al.*, 1984; Little *et al.*, 1987). These rates are enormously rapid on a geologic timescale, as are the rates of generation of new crust at ridges and the spreading of crust across ocean basins. The oldest crust in the present ocean basins is not much more than 200×10^6 years old, implying that the forces driving plate tectonics have produced at least 20 or so times the present volume of oceanic crust over the lifetime of the Earth (this value depends, of course, on past seafloor spreading rates and on the timing of the initiation of plate tectonics on the early Earth). The enormous amount of new crustal material created at divergent plate boundaries is matched by an equally enormous amount of altered crustal material and sediments subducted back into the mantle and accreted on the continents.

As newly generated oceanic crust spreads away from ridge crests it is cooled by circulating fluids which flow in a pattern of forced and free convection cells (Figs. 1 and 2). These fluids move through the crust at rates which generally exceed those at which newly

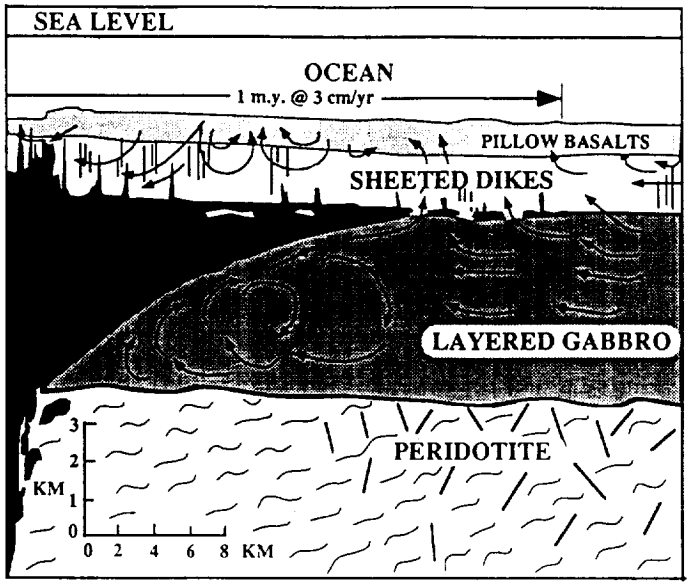

Fig. 1. (after Gregory and Taylor, 1981) Schematic cross section of oceanic crust at a spreading center based on petrologic and isotopic results from the Samail ophiolite in Oman. The dark region represents a hypothetical magma chamber which includes liquid and crystal-mush regions. Arrows indicate possible direction of fluid flow which penetrated to at least 6 km depth.

formed crust moves away from spreading centers. Depending on the rates of heat flow, local stress environments, chemical reactions and crustal structure, hydrothermal convection cells may remain more or less stationary in newly formed crust for thousands to millions of years. It should be kept in mind that oceanic crust moves laterally through these cells of convecting fluids over similar timescales. As a consequence, basalt which solidifies at the spreading center can be progressively altered by hydrothermal fluids for millions of years. The resulting geologic samples from ophiolite sequences or from drill holes in the seafloor contain the superimposed history of crustal formation and hydrothermal alteration.

The thermal and hydrologic histories which develop in these dynamic systems can be quite complex, and their accumulated products are often mixed and juxtaposed at any particular place in the altered oceanic crust. As an example, reference to Fig. 2 shows that basalt at approximately 1 km depth can pass through zones of high temperature (≥350°C) hydrothermal alteration, followed by low temperature (maybe ≤100°C) subseafloor weathering in zones of fluid recharge, and subsequent heating (temperatures up to ~250°C) in regions of fluid upwelling further off the axis of the spreading center. This pattern of oscillations can repeat in a somewhat dampened fashion until the fracture

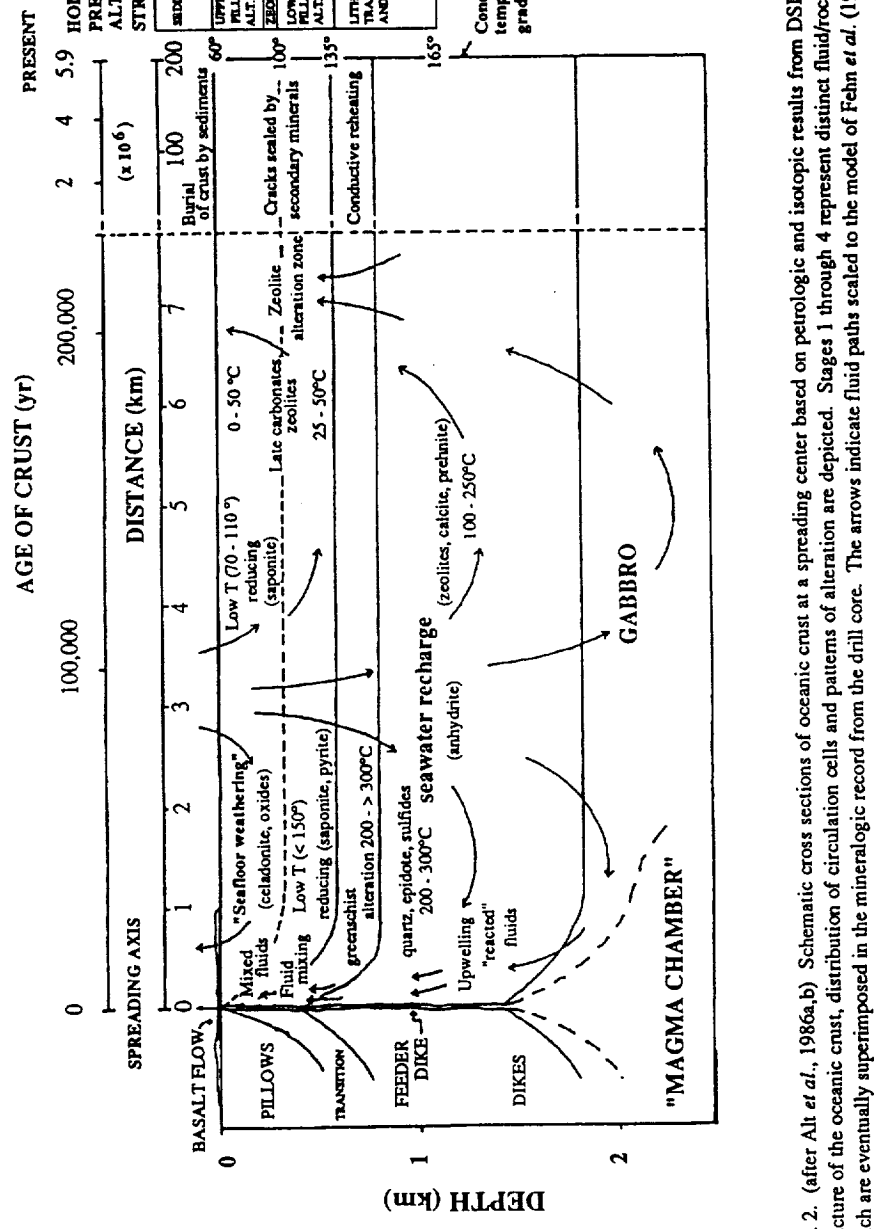

Fig. 2. (after Alt *et al.*, 1986a,b) Schematic cross sections of oceanic crust at a spreading center based on petrologic and isotopic results from DSDP site 504B. The structure of the oceanic crust, distribution of circulation cells and patterns of alteration are depicted. Stages 1 through 4 represent distinct fluid/rock alteration events which are eventually superimposed in the mineralogic record from the drill core. The arrows indicate fluid paths scaled to the model of Fehn *et al.* (1983).

network fills with secondary minerals and seals off. Although some crack sealing has occurred in core from Deep Sea Drilling Program (DSDP) hole 504B on the eastern flank of the Costa Rica Rift (Fig. 2), it is estimated that this process generally takes at least 60 to 80 million years to be completed based on the persistence of depressed heat flow in wide zones around the spreading centers (Anderson *et al.*, 1977). As fluid flow decreases, the crust will be more uniformly heated by conduction. Results from DSDP hole 504B indicate that temperatures in basalt at 1 km depth are ≥150°C even after nearly 6 million years of fluid circulation and alteration (Alt *et al.*, 1986a,b, 1989; Becker *et al.*, 1989).

3. Pressure and Temperature in Submarine Hydrothermal Systems

Hydrostatic pressures at the ocean/seafloor interface can be easily calculated from the depth of the overlying water column, the density of seawater, and the acceleration due to gravity. To the extent that fracture systems in seafloor sediments and basalt are open to the ocean/seafloor interface, pressures in fracture systems will also be hydrostatic. If geologic structures which serve as impermeable layers, such as fractures sealed with precipitated minerals, interfere with the permeability of geologic materials, the connectivity between aqueous fluids and the ocean/sediment interface can be blocked, and pressures can become lithostatic. In other words, the density of the overlying column of rock must be taken into account.

The fluid venting from black-smoker chimneys at mid-ocean ridges is connected through fracture systems to seawater and is at hydrostatic pressure. Fluids which are responsible for deep alteration of ophiolites (depths of 5 km or more) may have been at lithostatic pressures depending on the timing of fluid infiltration, the hydrodynamics of fracture systems, and the permeability of geologic materials (Gregory and Taylor, 1981). In either case, the fluid flows in response to buoyancy forces generated by the transfer of heat from the magma chamber to the hydrothermal fluid and the consequent fluctuation in fluid density (Norton, 1984). The rapid upward convection of these hot fluids can be thought to result from their relatively low density compared to the surrounding seawater.

Temperatures of aqueous fluids in submarine hydrothermal systems range from nearly 0°C at the seafloor to at least 700°C at depths of 3 km (Vanko, 1988). Higher temperature alteration (up to 900°C) has been documented in ophiolite sequences (Kimball, 1988), and is suggested in results from Ocean Drilling Program (ODP) site 735B (see below). Alteration of basalts, gabbros and other oceanic crustal rocks by hydrothermal fluids is generally more conspicuous at temperatures < 600°C than at higher temperatures. At the lower temperature range, the alteration occurs within the thermodynamic stability fields of several hydrous minerals (chlorite, talc, epidote, amphiboles, etc.) which are absent or uncommon in freshly crystallized oceanic igneous rocks. Although direct petrolgraphic evidence for hydrothermal alteration becomes more cryptic at higher temperatures (Norton and Taylor, 1979; Bird *et al.*, 1986, 1988; Schiffries and Skinner, 1987),

oxygen isotopic data on samples from ophiolites indicate that pervasive hydrothermal alteration occurs to at least 6 km depths in the ocean crust (Gregory and Taylor, 1981; Cocker *et al.*, 1982; Ito and Clayton, 1983; Stakes *et al.*, 1983).

Studies of fluid inclusions, small fluid samples trapped within minerals which have precipitated during hydrothermal alteration, indicate that high-salinity brines (equivalent to 30 to 60 wt % NaCl) are generated deep in submarine hydrothermal systems (Kelley and Delaney, 1987; Cowan and Cann, 1988; Vanko, 1988; Kelley and Robinson, 1990; Nehlig, 1991). One explanation for the origin of these brines is phase separation above the consulate point in the H_2O-NaCl system at seawater salinities (Kelley and Delaney, 1987). Supporting evidence for phase separation in submarine hydrothermal systems comes from observations of Axial Seamount on the Juan de Fuca Ridge where fluids with dramatically different salinities, metal contents, and concentrations of dissolved gases vent from hot springs in close proximity (Massoth *et al.*, 1989; Butterfield *et al.*, 1990).

High temperatures in submarine hydrothermal systems are reached near the magma chamber during generation of new crustal material, but the duration of high-temperature alteration is likely to be shorter than lower-temperature alteration which continues for millions of years. Fluids circulate through a band of oceanic crust hundreds of kilometers wide around mid-ocean ridges (COSOD II, 1987), and at any moment the majority of these fluids are at temperatures considerably lower than those near the magma chamber or those flowing from hydrothermal vents. Recent estimates indicate that flow of warm water from the flanks of mid-ocean ridges is about 560 km^3 $year^{-1}$ (± a factor of 3), or more than 20 times greater than flow from the ridge-crest hydrothermal vents (24 km^3 $year^{-1}$, COSOD II, 1987). The mass of fluid exiting the flanks is enormous and probably in the range 100 to 1000 x 10^{12} kg $year^{-1}$. If hydrothermal organic synthesis reactions can produce 1 ppm organic carbon in these solutions, the annual yield would be between 10^8 and 10^9 kg.

4. The Properties of H_2O at the Pressures and Temperatures of Submarine Hydrothermal Systems

Pressures from a few hundred bars to several kilobars and temperatures from 2°C (deep seawater) to at least 900°C can be encountered in submarine hydrothermal systems. These conditions are represented on the axes of Fig. 3 which contains a phase diagram for the system H_2O. The solid curve in Fig. 3 separates the liquid and vapor stability fields for H_2O. This curve terminates at the critical point of H_2O (373.917°C, 220.46 bar) beyond which H_2O is a single supercritical phase. At the critical point, the density of H_2O is 0.322778 gm cm^{-3} (Johnson and Norton, 1991). The dashed line extending from the critical point indicates the location of densities equal to this critical value (the critical isochore) which can be thought of as a boundary between the liquid-like and vapor-like regions of the single-phase, supercritical H_2O. The critical point of seawater, which should be referred to as a consulate point, is somewhat higher than that of pure H_2O owing to the

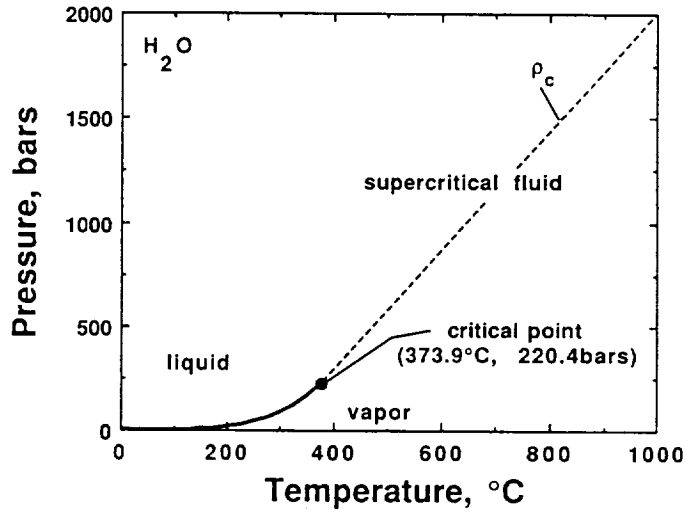

Fig. 3. Pressure/temperature phase diagram for the system H_2O showing the two phase (boiling) curve, critical point and location of the critical isochore (ρ_c). The triple point of H_2O and ice stability fields are omitted for clarity.

colligative properties of salt solutions. One recent estimate by Bischoff and Rosenbauer (1988) places the consulate point of seawater at 407°C and 298.5 bars. As in the case of the H_2O system, vapor-liquid phase separation occurs along the two-phase curve at conditions below this consulate point. Above the consulate point along the two-phase curve for the system H_2O-NaCl, phase separation yields a water-rich liquid and an NaCl-rich brine (Bischoff and Pitzer, 1989).

Although the density, and therefore the molar volume (V), of H_2O is finite at the critical point (see Fig. 4), the pressure and temperature derivatives of the density approach ∞. This can be illustrated by plotting values of the coefficient of isobaric expansivity, α, given by

$$\alpha \equiv \frac{1}{V}\left(\frac{\partial V}{\partial T}\right)_P \tag{1}$$

and the coefficient of isothermal compressibility, β, defined by

$$\beta \equiv -\frac{1}{V}\left(\frac{\partial V}{\partial P}\right)_T \tag{2}$$

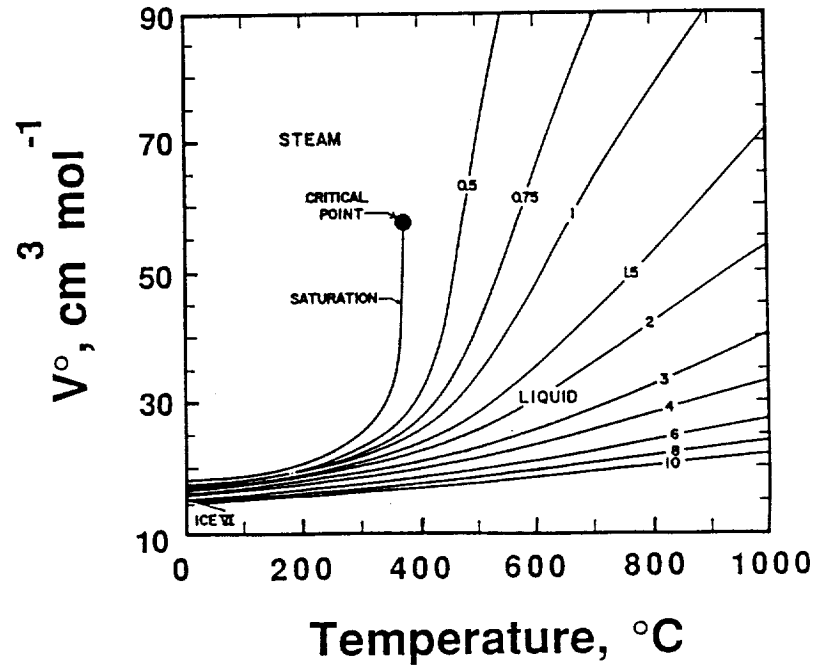

Fig. 4. (after Helgeson and Kirkham, 1974a) The molal volume of H_2O as a function of temperature at various pressures labeled in kilobars.

as functions of pressure and temperature. Plots of this type are shown in Figs. 5 and 6, where it can be seen that values of α and β increase dramatically with increasing temperature along the vapor-liquid saturation curve for H_2O. The isobaric molal heat capacity of H_2O also approaches ∞ at the critical point as inferred from the plot in Fig. 7.

Johnson and Norton (1991) have provided a unified equation of state for H_2O which allows accurate representation of these and many other properties in the region of pressure/temperature space around the critical point of H_2O. These authors also evaluate the extrema in dynamic viscosity, thermal conductivity, kinematic viscosity, thermal diffusivity and Prandtl numbers in the critical region, all of which are used to evaluate the physical properties of fluid flow. These extrema in transport and thermodynamic properties of H_2O in the critical region help to explain why hydrothermal circulation is particularly vigorous and effective in the critical region (Norton and Knight, 1977; Norton, 1984, 1990; Taylor, 1990). These effects are summarized by Taylor (1990) who states that in the critical region, "the buoyancy and heat transport properties of the fluid are maximized and drag forces are minimized", and that "it is very likely that these physical properties of

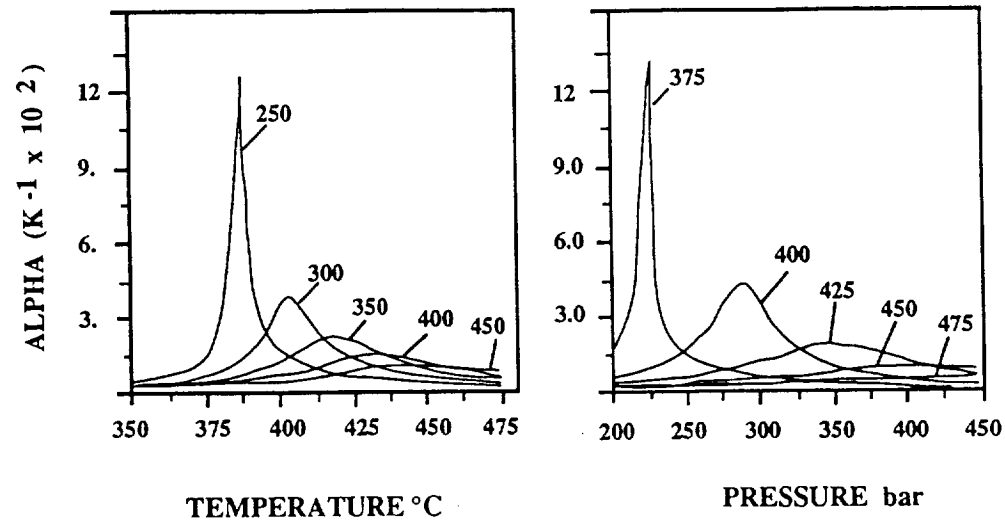

Fig. 5. (after Johnson and Norton, 1991) Isobaric expansivity of H_2O as a function of temperature and pressure in the vicinity of the critical point.

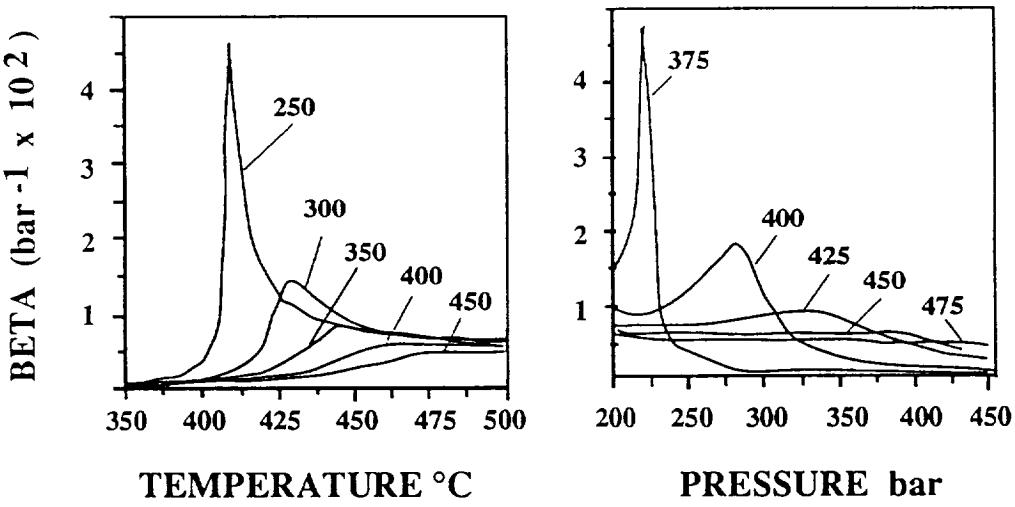

Fig. 6. (after Johnson and Norton, 1991) Isothermal compressibility of H_2O as a function of temperature and pressure in the vicinity of the critical point.

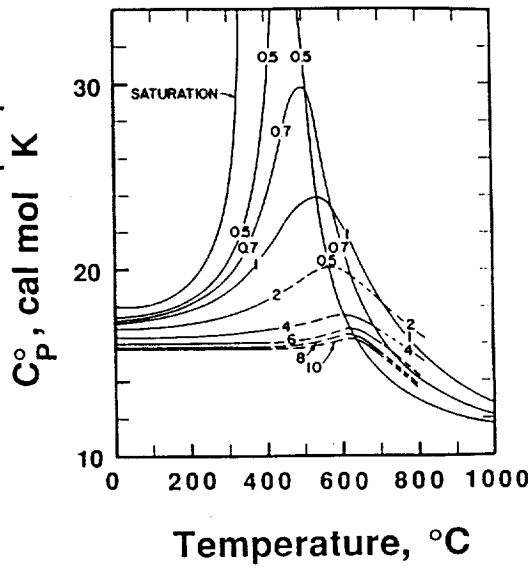

Fig. 7. (after Helgeson and Kirkham, 1974a) The standard molal isobaric heat capacity of H_2O as a function of temperature a various pressures labeled in kilobars.

H_2O control the observed upper limit of 350° to 400°C observed during surface venting of modern hydrothermal systems."

The effects of hydrothermal fluids on the basalts and layered gabbros of the oceanic crust are recorded by assemblages of alteration minerals. The ability of hydrothermal fluids to transport ions and other aqueous species into and away from zones of alteration is strongly correlated with changes in the electrostatic properties of the fluid. As shown in Fig. 8, the dielectric constant of H_2O decreases steadily from a value of ~ 80 at 25°C and 1 bar to ~ 7 at the critical point. It can also be seen in Fig. 8 that pressure has a mild effect on the dielectric constant, and that values less than the critical value are attained in the supercritical region. Also shown along the right-hand vertical axis of Fig. 8 are values of the dielectric constant for several organic solvents at 25°C and 1 bar, emphasizing the point that H_2O is an enormously different solvent at hydrothermal conditions than it is at typical laboratory conditions. This observation may be particularly important for considerations of H_2O-organic compound reactions at hydrothermal conditions (Shock and Helgeson, 1990; Siskin and Katritzky, 1991).

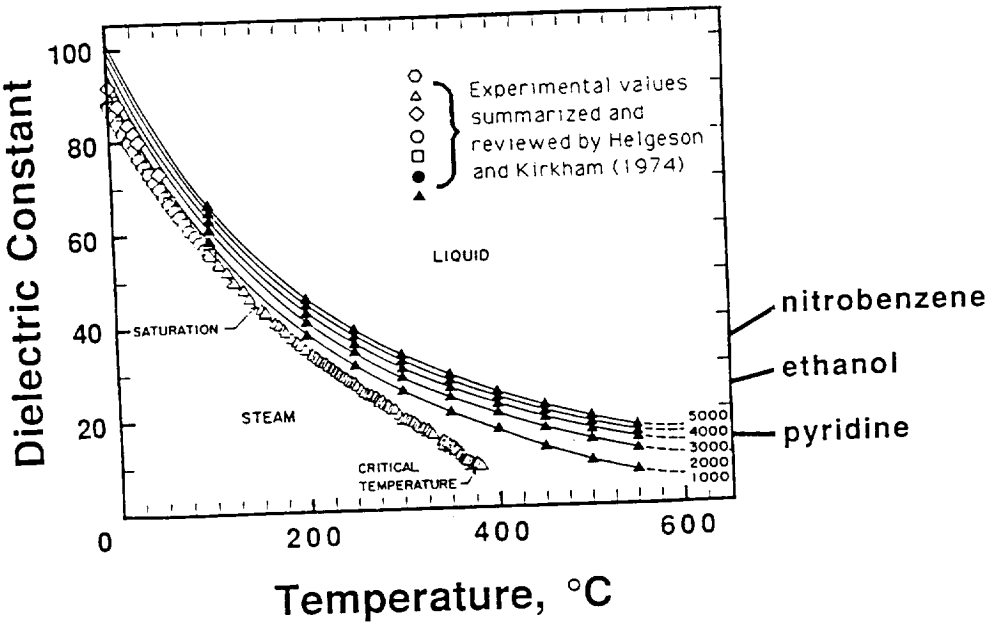

Fig. 8. (after Helgeson and Kirkham, 1974a) The dielectric constant of H_2O as a function of temperature at various pressures labeled in bars.

5. Thermodynamic Properties of Aqueous Species and Reactions at High Pressures and Temperatures

The fluctuations in the thermodynamic, transport and electrostatic properties of H_2O described above can be used to evaluate thermodynamic and transport properties of aqueous species, as well as thermodynamic properties of reactions among aqueous species and between aqueous species, minerals, organic compounds and gases. One approach to evaluating thermodynamic properties of aqueous species at elevated pressures and temperatures which is widely applicable in the study of hydrothermal systems involves the Helgeson-Kirkham-Flowers equations of state and their recent revisions (Helgeson and Kirkham, 1976; Helgeson, Kirkham and Flowers, 1981; Tanger and Helgeson, 1988; Shock *et al.*, 1992). Thermodynamic data and equation-of-state parameters for hundreds of inorganic and organic species are presently available (Shock and Helgeson, 1988, 1990; Shock *et al.*, 1989; Sassani and Shock, 1990a, 1992; Sverjensky *et al.*, 1992; Shock, 1992a,c,d,e). These data and parameters allow calculations to 1000°C and 5 kb. The accuracy and generality of these equations, data and parameters are demonstrated by the comparisons between calculations (solid curves) and experimental data (symbols) in

Figs. 9-11. The examples selected include many aqueous species of interest to the study of organic synthesis in hydrothermal systems.

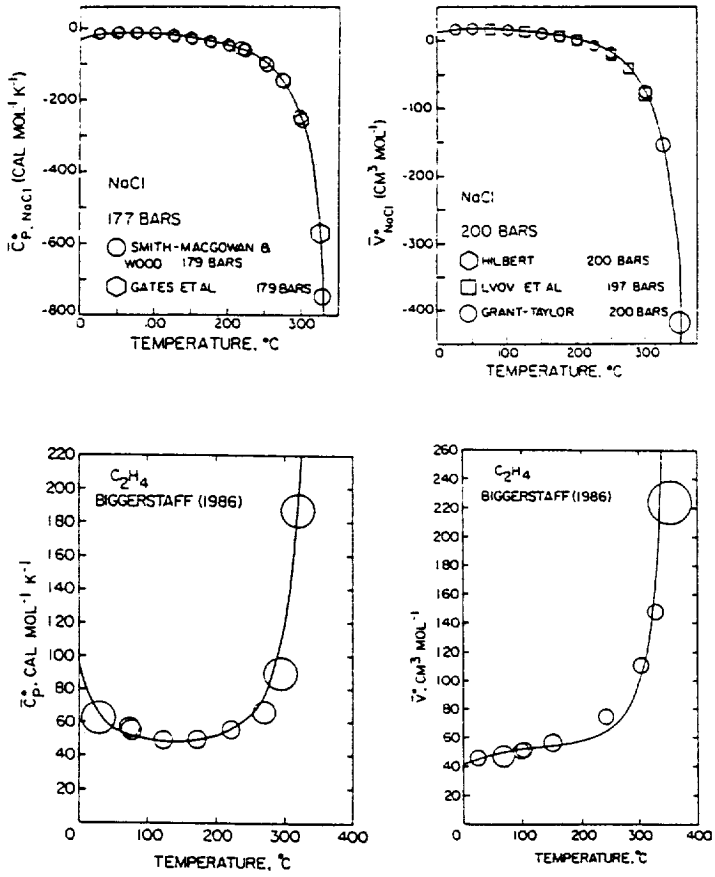

Fig. 9. (after Shock *et al.*, 1989, 1992) Plots of the standard partial molal heat capacity ($\overline{C_p}^\circ$) and volume ($\overline{V}^\circ$) of NaCl and C_2H_4 in aqueous solution as functions of temperature at constant pressure. Symbols represent experimental data from the references indicated, and curves correspond to regression results with the revised HKF equations of state (see text).

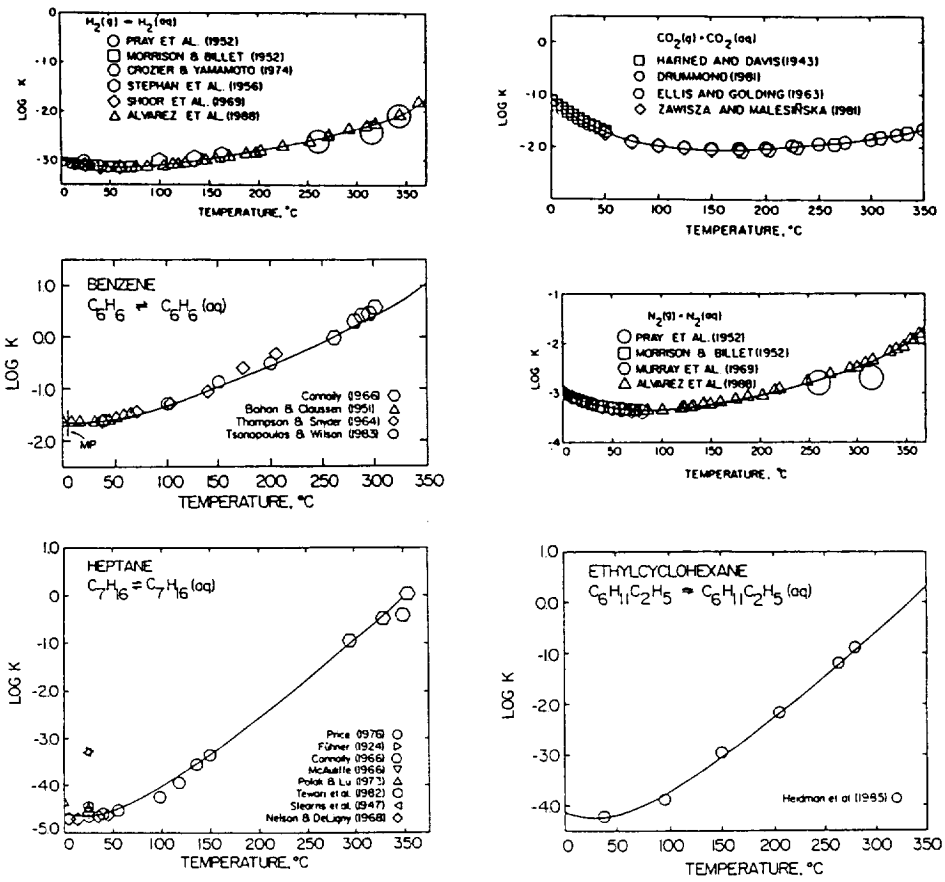

Fig. 10. (after Shock *et al.*, 1989; Shock, 1992f) Plots of standard state equilibrium constants for solubility reactions for H_2, CO_2, N_2, benzene, heptane and ethylcyclohexane. Symbols represent experimental data from the references indicated, and curves correspond to values calculated with the revised HKF equations of state (see text).

5.1. INORGANIC AND ORGANIC IONS AND ELECTROLYTES

Standard partial molal volumes ($\bar{V}^\circ$), isobaric heat capacities ($\bar{C}p^\circ$), and entropies ($\bar{S}^\circ$), as well as apparent standard partial molal enthalpies of formation ($\Delta\bar{H}_f^\circ$) of aqueous ions and electrolytes approach $-\infty$ at the critical point of H_2O. This behavior is a direct consequence of ion solvation which in turn reflects the temperature and pressure dependence of the dielectric constant of H_2O (Helgeson and Kirkham, 1974b, 1976). Experimental evidence of this behavior is indicated by the symbols shown in Fig. 9 for $\bar{V}^\circ$ and $\bar{C}p^\circ$ of the electrolyte NaCl. The curves in Fig. 9 are calculated with the revised

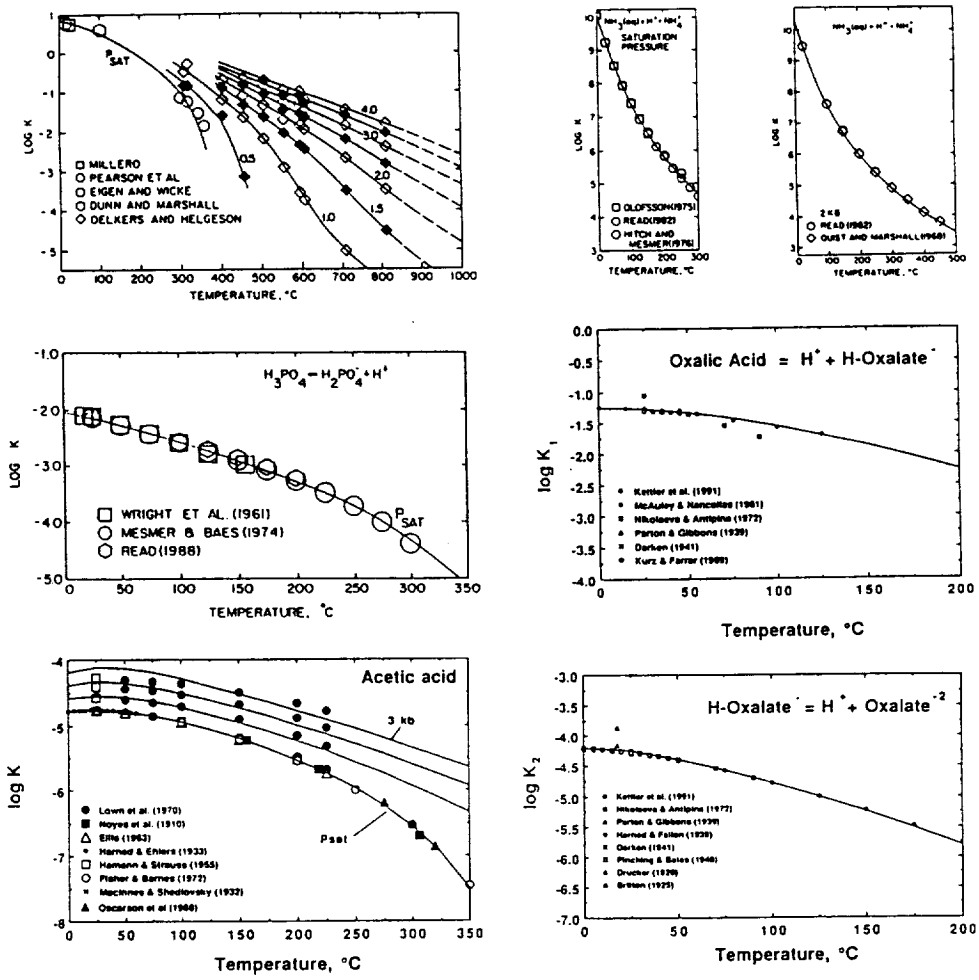

Fig. 11. (after Shock *et al.*, 1989, 1992; Shock, 1992d) Plots of equilibrium constants for complex and acid dissociation reactions of NaCl, H_3PO_4, oxalic and acetic acids, as well as for the protonation of NH_3. All log K values are plotted as functions of temperature at the saturation pressure or at higher pressures labeled in kilobars. Symbols represent experimental data from the references indicated, and the curves are calculated with the revised HKF equations of state (see text).

Helgeson-Kirkham-Flowers (HKF) equations of state (Helgeson *et al.*, 1981; Tanger and Helgeson, 1988; Shock *et al.*, 1992). Parameters in these equations are obtained by regression of experimental data and by application of correlation algorithms, and are available for hundreds of inorganic and organic ions (Shock and Helgeson, 1988, 1990; Sassani and Shock, 1990a; Shock, 1992d). These parameters, together with standard state

thermodynamic data for the ions at 25°C and 1 bar allow calculation of the corresponding thermodynamic properties of ions to 1000°C and 5kb.

5.2. INORGANIC AND ORGANIC NEUTRAL SPECIES

In contrast to aqueous ions and electrolytes, $\bar{V}^\circ$, $\bar{C}p^\circ$, $\bar{S}^\circ$, and $\Delta\bar{H}_f^\circ$ of many aqueous neutral species approach ∞ at the critical point of H_2O. Experimental evidence of this behavior is shown by the symbols representing $\bar{V}^\circ$ and $\bar{C}p^\circ$ for aqueous ethylene in Fig. 9. The curves in Fig. 9 were generated with the revised HKF equations of state (Shock and Helgeson, 1990; Shock *et al.*, 1992). The approach of standard partial molal properties of neutral species to ∞ is typical behavior for those species which in pure form exist as gases or supercritical fluids at the critical point of H_2O. Neutral species which have solid-phase analogs at the critical point of H_2O, such as aqueous silica for which the pure analog is quartz, will exhibit behavior like aqueous ions. Regression of gas solubility and quartz solubility data (Shock *et al.*, 1989) provides standard state data and equation-of-state parameters for numerous neutral aqueous species including many organic compounds (Shock and Helgeson, 1990; Shock, 1992f). Comparisons of experimental gas and hydrocarbon solubility data with calculations performed with the revised HKF equations of state are depicted in Fig. 10. The close agreement between experimental and calculated values of log K for solubility reactions provides the framework for regressing dissociation constant data for acids and aqueous complexes such as $NaCl^\circ$, which are also neutral aqueous species.

5.3. COMPLEX ASSOCIATION AND ACID DISSOCIATION

Dissociation constants for the reaction

$$NaCl^\circ = Na^+ + Cl^- \qquad (3)$$

are shown in Fig. 11 where the symbols designate experimental values and the curves correspond to calculations with the revised HKF equations of state (Shock *et al.*, 1992). Data for numerous other neutral and charged inorganic aqueous complex dissociation reactions were regressed by Sverjensky *et al.* (1992), who provide a general framework for predicting dissociation constants at elevated temperatures and pressures which have not been measured experimentally. As a consequence, it is now possible to make a detailed accounting of the speciation of major and trace elements in hydrothermal fluids to 1000°C and 5kb (see for example: Molling and Sverjensky, 1989; Sassani and Shock, 1990a,b; Sverjensky, 1991; Willis and Shock, 1991). Speciation calculations allow evaluation of total concentrations of elements in hydrothermal fluids from ion activity ratios obtained from consideration of mineral/fluid reactions.

Acid dissociation reactions are treated in a manner analogous to complexes. Equilibrium constants obtained from experiments are regressed with the revised HKF equations of state to obtain the equation-of-state parameters that are used to construct correlations which, in turn, allow estimates for the many acids which have not been studied experimentally (Shock *et al.*, 1989; Shock and Helgeson, 1990; Shock, 1992d). Close agreement between experimental and calculated values of acid dissociation constants is demonstrated in Fig. 11 for acetic acid, oxalic acid, and H_3PO_4, as well as for the protonation of aqueous NH_3.

5.4. OXIDATION/REDUCTION REACTIONS

Thermodynamic data and equation of state parameters for aqueous species provide the means of evaluating the magnitude of the driving force for organic synthesis at hydrothermal conditions (Shock, 1990a,b). As an example, let us consider the potential synthesis of acetic acid in submarine hydrothermal systems. The predominant inorganic form of volatile carbon leaving the mantle is likely to be CO_2 (see below). Synthesis of acetic acid will require reduction of CO_2 through an overall reaction of the type

$$2\,CO_2\,(g) + 4\,H_2(g) = CH_3COOH(aq) + 2\,H_2O\ . \tag{4}$$

We can write the expression of the law of mass action for this reaction as

$$K_4 = \frac{a\,(CH_3CHOOH)\,a^2(H_2O)}{f^2(CO_2)\,f^4(H_2)}, \tag{5}$$

where K_4 designates the equilibrium constant for reaction (4), a stands for activity and f represents fugacity. Activities of H_2O rarely stray far from unity in hydrothermal fluids except at extremes of concentration (Helgeson, 1979, 1985). Taking the logarithm of Eqn. (5) with this in mind allows us to write

$$\log fCO_2 = 2\log fH_2 + \frac{1}{2}\,(\log a\,CH_3COOH - \log K_4)\ , \tag{6}$$

which corresponds to an equation of a line on a plot of $\log fCO_2$ vs $\log fH_2$. Such a plot is shown in Fig. 12 constructed for 150°C and 500 bars, where $\log K_4 = 0.18$ (Shock, 1992c).

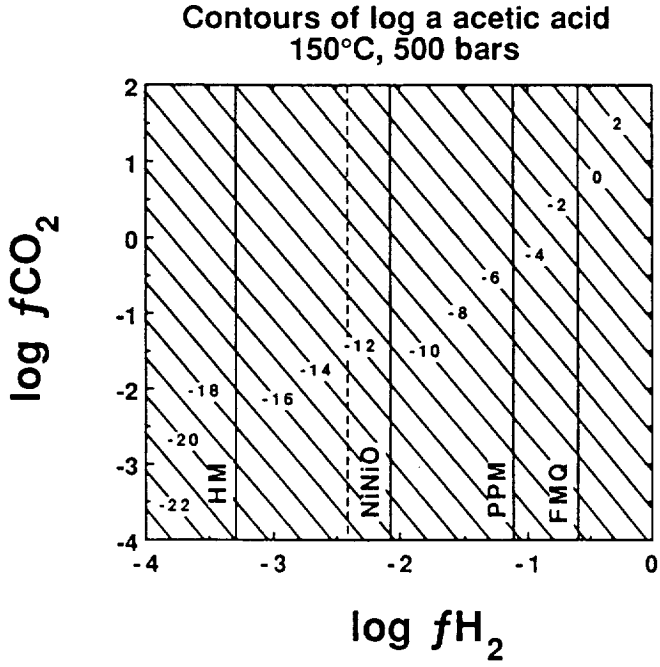

Fig. 12. Fugacity diagram showing contours of log a acetic acid in fH_2-fCO_2 space at 150°C and 500 bars. Vertical lines show positions of various mineral buffers of fH_2 (reactions 7 - 10) at the same temperature and pressure.

Contours of log a CH_3COOH are shown in Fig. 12 together with the locations of mineral redox buffer assemblages corresponding to the hematite-magnetite (HM), nickel-nickel oxide (NiNiO), pyrite-pyrrhotite-magnetite (PPM) and fayalite-magnetite-quartz (FMQ) reactions given by

$$\underset{\text{magnetite}}{2\,Fe_3O_4} + H_2O = \underset{\text{hematite}}{3\,Fe_2O_3} + H_2(g)\ , \tag{7}$$

$$Ni + H_2O = NiO + H_2(g)\ , \tag{8}$$

$$\underset{\text{pyrrhotite}}{1.5\,FeS} + H_2O = \underset{\text{pyrite}}{0.75\,FeS_2} + \underset{\text{magnetite}}{0.25\,Fe_3O_4} + H_2(g)\ , \tag{9}$$

and

$$\underset{\text{fayalite}}{1.5\,Fe_2SiO_4} + H_2O = \underset{\text{magnetite}}{Fe_3O_4} + \underset{\text{quartz}}{1.5\,SiO_2} + H_2(g)\ . \tag{10}$$

It can be seen in Fig. 12 that the activity of acetic acid is $\sim 10^{-2}$ at equilibrium with 10 bars of CO_2 and the log fH_2 values set by the PPM assemblage at 150°C and 500 bars. The activity of acetic acid is high because CO_2 is unstable at this fH_2 value as indicated by the location of the dashed line which represents the fH_2 value corresponding to equal fugacities of CO_2 and CH_4 if stable equilibrium attains. If stable equilibrium between CO_2 and CH_4 is blocked by kinetic barriers in hydrothermal systems, then metastable organic synthesis may prevail (Shock, 1990b, see below).

Results of speciation calculations conducted to test the possibility of hydrothermal organic synthesis are described below. In contrast to the calculations used to construct Fig. 12, speciation calculations account for mass-balance constraints together with consideration of simultaneous metastable equilibrium constraints for several possible products of reactions like Eqn. (4). Any attempt to constrain such calculations, or experiments which simulate submarine hydrothermal systems, must take into account the buffering capacity of fluid/rock reactions.

6. Fluid/Rock Reactions in Submarine Hydrothermal Systems

Taken together, studies of hydrothermal vent fluids, ophiolites, volcanogenic sulfide ore deposits, and samples from DSDP and ODP sites like 504B and 735B yield a detailed picture of the products of fluid/rock reactions in submarine hydrothermal systems (Bischoff and Seyfried, 1978; Edmond *et al.*, 1979a,b, 1982, 1987; Zierenberg *et al.*, 1984, 1988; Merlivat *et al.*, 1987; Shanks and Seyfried, 1987; Richardson *et al.*, 1987; Kadko and Moore, 1988; Kawahata and Shikazono, 1988; Woodruff and Shanks, 1988; Campbell *et al.*, 1988a,b; Harper *et al.*, 1988; Alt *et al.* 1989; Becker *et al.*, 1989; Hayman, 1989; Campbell and Edmond, 1989; Berndt and Seyfried, 1990; Von Damm, 1990; Dick *et al.* 1991; among many others). These observations can be coupled with experimental studies (Seyfried and Bischoff, 1977, 1979, 1981; Mottl and Seyfried, 1980; Hajash and Chandler, 1981; Seyfried and Mottl, 1982; Janecky and Seyfried, 1986; Shiraki *et al.*, 1987; Seyfried, 1987; Cole *et al.*, 1987; Bischoff and Rosenbauer, 1983, 1987; Thornton and Seyfried, 1987; Seyfried *et al.*, 1987, 1988; Berndt *et al.*, 1988, 1989; Seewald and Seyfried, 1990; among others), and theoretical calculations of the dynamics of fluid flow and chemical mass transfer to reveal many of the hydrologic, thermodynamic and kinetic factors which control mineral alteration and compositional changes in fluids (Fehn *et al.*, 1983; Haymon, 1983; Mottl, 1983; Reed, 1983; Janecky and Seyfried, 1984; Bowers and Taylor, 1985; Seyfried and Janecky, 1985; Bowers *et al.*, 1985, 1988; Von Damm, 1988; Janecky and Shanks, 1988; Goldfarb and Delaney, 1988; Cann and Strens, 1989; Brikowski and Norton, 1989; Bowers, 1989; Fox, 1990; Norton, 1990; Lowell, 1990, 1991; Fisher *et al.*, 1990; Tivey and McDuff 1990; Fisher and Becker, 1991; Fisher and Narasimhan, 1991; Lowell and Burnell, 1991; among many others). These same factors are likely to control, or strongly influence, possible organic synthesis in submarine hy-

drothermal systems. Evidence is reviewed in this section for controls on pH, oxidation state and major element composition in these systems.

6.1. MINERAL ALTERATION

The original igneous mineral assemblages of oceanic crust are replaced to varying extents during hydrothermal alteration. Evidence for alteration of oceanic crust at temperatures from 0° to 900°C comes from drill core, dredge samples and ophiolite sequences (Coish, 1977; Humphris and Thompson, 1978; Böhlke *et al.*, 1981; Oudin and Constantinou, 1984; Mevel, 1987, 1988; Schiffman *et al.*, 1987; Delaney *et al.*, 1987; Vanko, 1988; Schiffman and Smith, 1988; Silant'yev *et al.*, 1988; Schöps and Herzig, 1990; Dick *et al.*, 1991; among many others). Fig. 13 contains a stratigraphic section through the Josephine ophiolite of California and Oregon together with the occurrence of various minerals (Harper, 1986; Harper *et al.*, 1988). Mineral formulas are given in Table 1. Note that most of the original igneous minerals are replaced, especially throughout the middle depths. These petrogenetic relations are quite similar to those recorded in a detailed study of core samples from DSDP site 504B. Stratigraphic data and assemblages of secondary minerals reported by Alt *et al.* (1986a, 1989) from 504B are shown in Fig. 14. Comparison of the lists and distribution of minerals in Fig. 13 and 14 indicates that chlorite, albite, epidote, actinolite, magnetite and quartz are among the most common alteration products in the deeper portions of the hydrothermally altered sequences. Note that pyrite and magnetite coexist through many hundred meters of oceanic crust as shown in Fig. 14. At shallower depths, many low-temperature alteration products are found including pumpellyite, aragonite, phillipsite, saponite, celadonite, and Fe-hydroxides.

Recently, the Ocean Drilling Program was successful in drilling 500 meters into oceanic layered gabbros located on the Southwest Indian Ridge at Site 735B (Robinson *et al.*, 1991; Dick *et al.*, 1991). Evidence for high-temperature metamorphism (Cannat *et al.*, 1991) as well as hydrothermal vein assemblages (Stakes *et al.*, 1991) attest to the presence of aqueous fluids at temperatures to at least 700°C, and that they may have been present at 900°C (Stakes *et al.*, 1991; Dick *et al.*, 1991). Isotopic data on oxygen and hydrogen (Stakes *et al.*, 1991; Kempton *et al.*, 1991), strontium (Kempton *et al.*, 1991), and sulfur (Alt and Anderson, 1991) also indicate pervasive high-temperature alteration. In addition, fluid inclusions in plagioclase, hornblende, diopside, apatite and quartz are present in these samples (Vanko and Stakes, 1991). The combined evidence from assemblages of alteration minerals and fluid inclusions indicates that early development of hornblende in the metagabbro occurred at ~720°C, followed by hornblende-plagioclase vein formation at 500° to 600°C, and retrograde greenschist alteration at temperatures below 400°C. Veins containing plagioclase and diopside appear to have formed at ~500°C and 1kb (Vanko and Stakes, 1991).

At the higher temperatures and pressures at which submarine hydrothermal fluids equilibrate with layered gabbros, peridotites and other mafic and ultramafic rocks, consid-

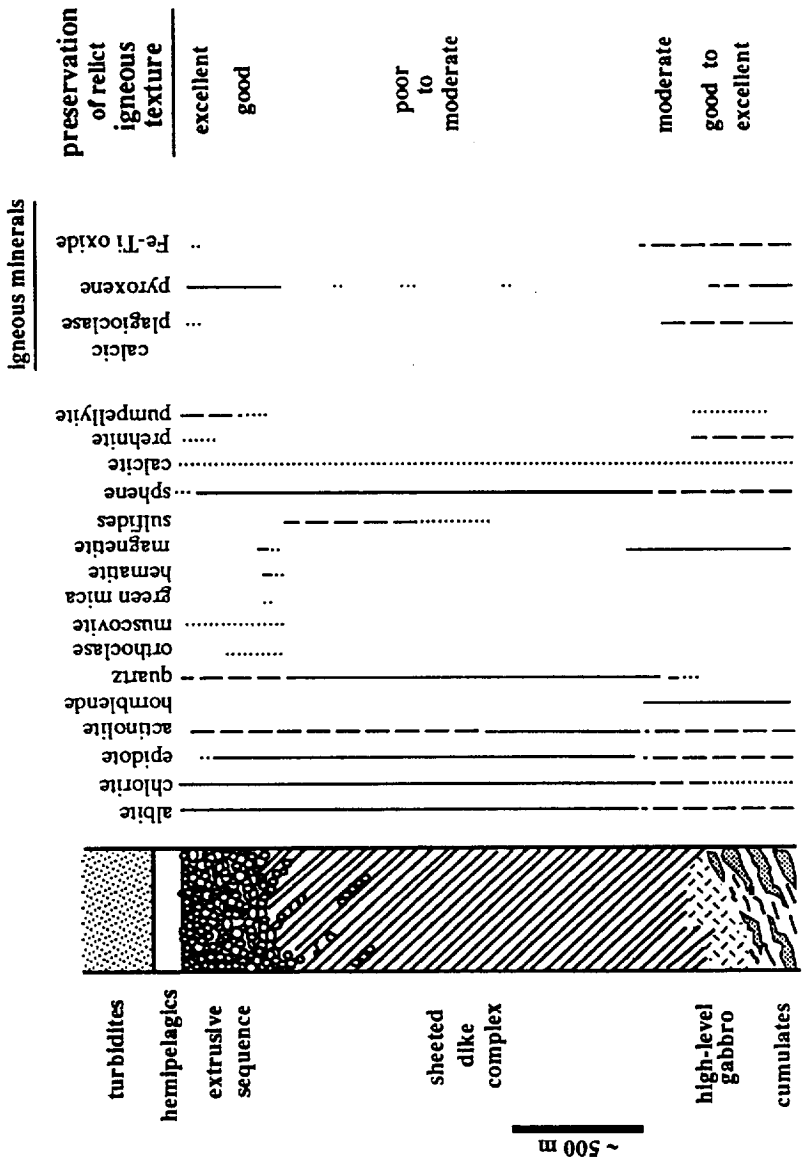

Fig. 13. (after Harper *et al.*, 1988) Lithostratigraphy and mineralogy vs. depth in the Josephine ophiolite. A solid line indicates that a mineral is characteristically present, a dashed line indicates that a mineral is commonly present and a dotted line indicates a minor or sporadic phase.

TABLE 1

Minerals in submarine hydrothermal systems refered to in the text and/or Figs. 13 and 14 and their formulas

Mineral Name	Formula
albite	$NaAlSi_3O_8$
analcite	$NaAlSi_2O_6 \cdot H_2O$
anhydrite	$CaSO_4$
apatite	$Ca_5(PO_4)_3(OH,F,Cl)$
apophyllite	$KCa_4Si_8O_{20}F \cdot 8\,H_2O$
aragonite	$CaCO_3$
celadonite	$KMgFeSi_4O_{10}(OH)_2$
chabazite	$CaAl_2Si_4O_{12} \cdot 6\,H_2O$
chalcopyrite	$CuFeS_2$
diopside	$CaMg(SiO_3)_2$
epidote	$Ca_2FeAl_2Si_3O_{12}(OH)$
fayalite	Fe_2SiO_4
galena	PbS
gyrolite	$Na(Ca, Mg, Fe)_{16}(Si, Al)_{24}O_{60}(OH) \cdot 15H_2O$
hematite	Fe_2O_3
magnetite	Fe_3O_4
mesolite	$Na_2Ca_2(Al_2Si_3O_{10})_3 \cdot 8\,H_2O$
muscovite	$KAl_2(AlSi_3)O_{10}(OH)_2$
natrolite	$Na_2Al_2Si_3O_{10} \cdot 2\,H_2O$
orthoclase	$KAlSi_3O_8$
prehnite	$CaAl(AlSi_3)O_{10}(OH)_2$
pyrite	FeS_2
pyrrhotite	FeS
quartz	SiO_2
sphalerite	ZnS
sphene	$CaTiSiO_5$
stilbite	$(Ca, Na_2, K_2)Al_2Si_7O_{18} \cdot 7\,H_2O$
talc	$Mg_3Si_4O_{10}(OH)_2$
thompsonite	$NaCa_2[(Al, Si)_5O_{10}]_2 \cdot 6\,H_2O$
tremolite	$Ca_2Mg_5Si_8O_{22}(OH)_2$

Mineral Group Names	Composition
actinolite	Ca, Mg, Fe amphibole
aegerine-augite	$(Na, Ca)(Fe, Mg)Si_2O_6$
chlorite	Mg, Fe, Al sheet silicate
hornblende	Na, Ca, Mg, Fe, Al amphibole
melanite	titanium-bearing garnet
phillopsite	Na, Ca, K zeolite
plagioclase	Na, Ca feldspar
pumpellyite	hydrous Ca, Mg, Fe, Al silicate
pyroxene	$(Mg, Fe)SiO_3$
saponite	Mg, Fe clay mineral

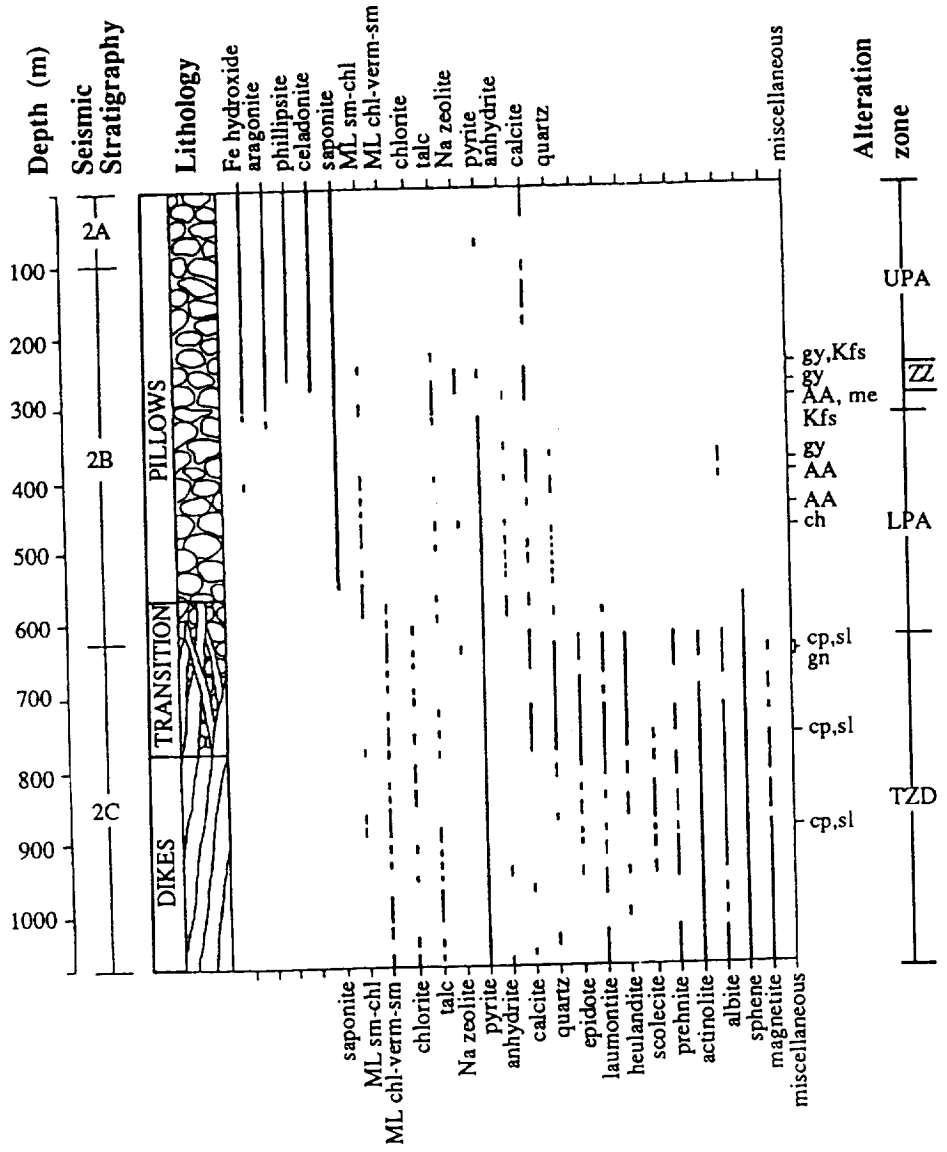

Fig. 14. (after Alt *et al.*, 1986a,b) Lithostratigraphy and distribution of alteration minerals in drill core from DSDP site 504B. Alteration zones correspond to those shown in Fig. 2. Depths given are below the overlying 274.5 m of sediment. ML sm-chl, mixed layer smectite-chlorite; ML chl-verm-sm, mixed layer chlorite-vermiculite-smectite; gy, gyrolite; AA, aegerine-augite; me, melanite; Kfs, K-feldspar; gn, galena; sl, sphalerite; cp, chalcopyrite; ch, chabazite. Na-zeolite includes analcite, stilbite, natrolite, mesolite, thomsonite, and apophyllite.

erable mass transfer is likely to occur. Preliminary mass-transfer calculations for reaction of 1.0 molal NaCl solutions initially at quartz saturation, with various mafic assemblages at 2kb and 400° to 750°C are reported by Sassani and Shock (1990b). In these calculations, pH values hover around neutrality, and the activities of the major rock-forming elements fluctuate over several orders of magnitude as a function of reaction progress. In addition, the resulting equilibrium mineral assemblages range from those containing ample talc, tremolite and other hydrous phases at lower temperatures (~500°C), to those consisting of strictly anhydrous, mafic minerals at higher temperatures (≥ 700°C). The latter differ from the mineral assemblages of the unaltered rocks, but might be (incorrectly) identified as being of strictly igneous origin since they lack obvious alteration phases. This type of cryptic alteration is probably common in rocks at great depths in the oceanic crust and upper mantle, and is consistent with oxygen isotopic measurements for ophiolites (Gregory and Taylor, 1981; Harper *et al.*, 1988). Cryptic alteration may already be documented in the samples from ODP site 735B.

6.2. MAJOR ION COMPOSITION OF SUBMARINE HYDROTHERMAL FLUIDS

The most thoroughly studied submarine hydrothermal fluids are those venting from hot springs on the ridge crest. Von Damm (1990) summarizes results from many investigators on 32 hot-spring samples with temperatures up to 380°C. Relative to seawater concentrations, Li, K, Rb, Cs, Be, Ca, B, Al, As, Se, Fe, Mn, Cu, Zn, Cd, Co, Ag, Pb, CO_2, CH_4, H_2S, SiO_2, ^3He, ^4He, and H_2 are generally enriched in hydrothermal vent fluids. Concentrations of Na and Cl show both depletions and enrichments relative to seawater values, and Mg, F, and sulfate appear to be greatly depleted. An overriding assumption in reports of vent fluid composition is that the Mg concentration is essentially zero in the vent fluids, and that any Mg in the sample results from contamination by ambient seawater during sampling. This assumption is based on results of basalt/seawater experiments at vent temperatures which indicate an enormous depletion of Mg at temperatures above 150°C (Seyfried and Bischoff, 1979). As a result, most analyses are referenced to zero Mg concentrations by subtracting the appropriate fraction of seawater. This approach can introduce difficulties owing to the possibility that not all the Mg is removed from fluids which vent at lower temperatures, and in identifying evidence of low and high temperature fluid mixing (Von Damm, 1990). In addition, it sometimes leads to reports of negative concentrations for sulfate in the hydrothermal fluids.

Theoretical mass-transfer and speciation calculations for hydrothermal vent fluids indicate that their composition can be explained by reactions with mineral assemblages containing epidote, plagioclase, chlorite, and quartz (Bowers *et al.*, 1985, 1988). This assemblage compares closely with the observations from the deeper position of DSDP site 504B (Fig. 14), suggesting that the venting fluids react with mineral assemblages at depth in the crust and move rapidly to the surface through ridge-crest hydrothermal systems.

6.3. pH BUFFERING DURING FLUID/ROCK REACTIONS

Measured values of pH for vent fluids at 25°C and 1 bar are in the range 3 to 4 for fluids venting from ridge crests without sediments (Michard *et al.*, 1983, 1984; Von Damm *et al.*, 1985a; Von Damm and Bischoff, 1987; Campbell *et al.*, 1988; Butterfield *et al.*, 1990; among others). In the case of fluids from hot springs in the Guaymas Basin, where there are ~500 meters of terrigenous and marine sediments above the ridge-crest basalt, the pH at 25°C and 1 bar is 5.9 (Von Damm et al., 1985b). It must be emphasized that these pH values may be quite different from those of the fluids at the temperatures and pressures of the vent environment which can not be measured directly.

Values of pH can be calculated by taking account of fluid speciation at the appropriate temperature and pressure. These calculations require equilibrium constants for the numerous major element complexes which may be present, as well as activity coefficients at the appropriate salinity. As described above, many of the thermodynamic data required for these calculations have been determined from experiments and many more can be estimated with a variety of correlation algorithms based on regression of data from those experiments. Calculated pH values for fluids from ridge crests without sediments are in the range 4.1 to 4.7 at the elevated temperatures of the hydrothermal vents (Bowers *et al.*, 1988). As shown in Fig. 15, neutral pH changes as a function of temperature and pressure, and it can be seen that the pH values of hydrothermal fluids are acidic by about 1 to 2 units at 350°C. Somewhat acidic conditions are likely to prevail at lower temperatures as well, depending on the intensity of hydrous alteration of basalt. If the early oceanic crust was more enriched in Mg and Fe than present day oceanic basalt, which may have been the case given the presence of komatiites early in Earth history (Nisbet, 1987), pH values may have been somewhat basic in the coexisting hydrothermal fluids (Janecky and Seyfried, 1986).

6.4. REDOX BUFFERING DURING FLUID/ROCK REACTIONS

Oxidation states of hydrothermal fluids are seldom determined by direct measurement, but are often calculated by assuming equilibrium between fluids and mineral assemblages. In the case of submarine hydrothermal vent fluids, dissolved H_2 has been measured and can be compared to values consistent with mineral buffer assemblages such as those represented by reactions (7-10). As an example, Evans *et al.* (1988) report concentrations of H_2 in hydrothermal vent fluids collected at the southern Juan de Fuca ridge. The vent fields are at 2300m depth (Von Damm, 1990) and the samples were collected at approximately 285°C. Concentrations of H_2 in the fluid samples range from 148 to 313μm. Using the zero Mg assumption, Evans *et al.* (1988) take account of the relative contributions of hydrothermal fluids and sea water to each sample and estimate that the concentrations of H_2 in the pure hydrothermal fluids range from 270 to 527μm.

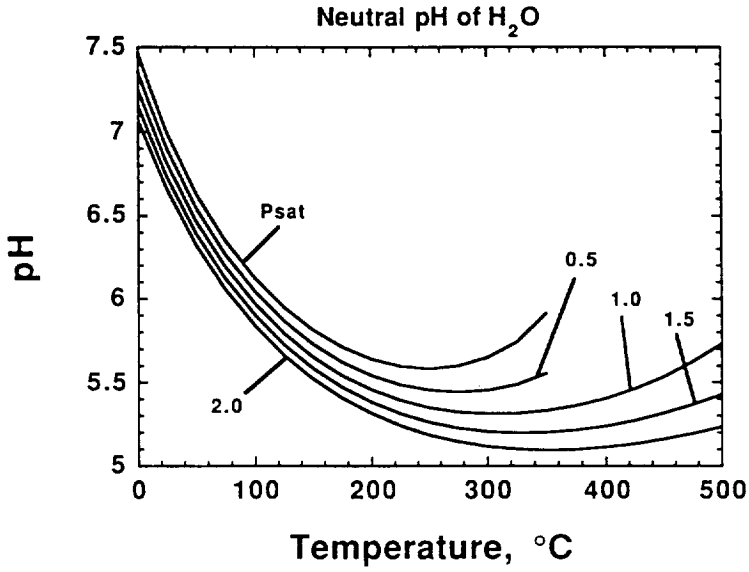

Fig. 15. Plot of neutral pH of pure H_2O as a function of temperature at the saturation pressure and higher pressures labeled in kilobars.

Fugacities of H_2 corresponding to these concentrations can be evaluated from calculated values of log K for the reaction

$$H_2(g) = H_2(aq) \quad (11)$$

using the computer code SUPCRT92 (Johnson *et al.*, 1992) which employs data, equations and parameters for H_2(aq) from Shock *et al.* (1989). Activity coefficients for H_2(aq) in hydrothermal fluids at these conditions have not been measured, so as a first approximation we can take molality and activity to be equivalent. The calculated log K for reaction 11 at 285°C and 230 bars is -2.52, and the log activities of H_2(aq) calculated from the samples range from -3.57 to -3.28. These values yield log fugacities of H_2 from -1.05 to -0.76, and the more positive of these values is in close agreement with the value of $\log f H_2 = -0.72$ set by the PPM assemblage at 285°C and 230 bars (also calculated with SUPCRT92). This result is consistent with the presence of these minerals in the hydrothermal vent chimney, plume and mineral deposits. Similar calculations for East Pacific Rise fluids by Janecky and Seyfried (1984) are also closely consistent with buffering by PPM as proposed by Hayman and Kastner (1981). Recent calculations by Roberts and Norton (1992) indicate that many measured vent-fluid compositions are consistent

with the coexistence of pyrite and magnetite but not pyrrhotite at 250 bars and 350°C. These results indicate that the fluids may be more oxidized than the PPM assemblage, consistent with the more negative values of $\log fH_2$ calculated above. As discussed in the next section, interplay between the temperature and the oxidation states of hydrothermal fluids are the factors which control whether metastable organic synthesis can occur in submarine hydrothermal systems.

7. The Potential for Organic Synthesis in Submarine Hydrothermal Systems

As emphasized elsewhere (Shock, 1990b), the crucial condition for organic synthesis in hydrothermal systems is the presence of kinetic barriers which block the attainment of stable thermodynamic equilibrium in the C-H-O-N system. If stable equilibrium is attained, the predominant species will be H_2O, H_2, CO_2, CH_4, graphite, N_2 and NH_3, and their relative abundances will be controlled by temperature, pressure and bulk composition (Dayhoff *et al.*, 1967; Holloway, 1984). At stable equilibrium in the C-H-O-N system the activities of organic compounds of interest to the study of the origin of life are minuscule. However, organic synthesis may proceed if kinetic barriers block stable equilibrium but allow metastable equilibrium states.

Evidence supporting the presence of kinetic barriers to stable equilibrium in the C-H-O-N system at hydrothermal conditions comes from isotopic studies of CO_2, CO, CH_4, N_2 and NH_3 (see: Shock, 1990b for a review). These data indicate that the lowest temperatures at which CO_2 and CH_4 equilibrate isotopically in submarine hydrothermal fluids is > 500°C (Welhan, 1988). At all lower temperatures there are kinetic barriers which prohibit equilibration of CO_2 and CH_4. Therefore, stable equilibrium is blocked in these systems.

Ample evidence from studies of organic acid concentrations in sedimentary basin brines, as well as consideration of reactions between organic acids, carbonate minerals and petroleum, indicates that metastable states among organic compounds and CO_2 are reached in oil reservoirs (Shock, 1988, 1989, 1992c; Helgeson and Shock, 1988; Helgeson *et al.*, 1991; Helgeson, 1991). These same calculations demonstrate that CH_4 and other light hydrocarbons are excluded from these metastable states. Therefore, it appears that *unlike* reactions between CO_2 and CH_4, those between CO_2, organic acids and petroleum hydrocarbons may *not* be hindered by kinetic barriers at temperatures from ~ 80° to 200°C or higher. As a consequence, the present understanding of reactions in the C-H-O-N system, based on a thermodynamic analysis of natural systems, is consistent with the possibility of organic synthesis from CO_2 and N_2 at hydrothermal conditions.

7.1. SOURCES OF CARBON AND NITROGEN

Identifying the inorganic forms in which carbon and nitrogen occur is essential in order to critically evaluate the potential for organic synthesis in submarine hydrothermal systems. So far, little is known about nitrogen in present-day hydrothermal vent fluids except those in the Guaymas Basin which contain from 10 to 15 mmol kg^{-1} NH_4^+. In this location, the origin of the ammonium is thought to be from organic matter in the 500 meters of sediments overlying the ridge (Von Damm, 1990).

Considerably more is known about volatile forms of inorganic carbon in present-day hydrothermal vent fluids. Those from the southern Juan de Fuca ridge contain ~ 4 mmol kg^{-1} CO_2, those at 21°N ~ 6 mmol kg^{-1}, those at the Galapagos spreading center ~ 10 mmol kg^{-1} and those at 11 - 13 °N on the East Pacific Rise ~ 15 mmol kg^{-1} (Von Damm, 1990). In contrast, fluids venting from the Virgin Mound on the Axial Volcano on the Juan de Fuca ridge contain ~ 285 mmol kg^{-1} CO_2 (Butterfield *et al.*, 1990). Methane and short-chain hydrocarbon concentrations are much lower than CO_2 concentrations at spreading centers without sediments such as the Southern Juan de Fuca ridge (Evans *et al.*, 1988; Welhan, 1988). Methane and other light hydrocarbons are abundant in hydrothermal fluids from sedimented ridges (Welhan and Lupton, 1987), as well as in the hydrothermal petroleum which is characteristic of these systems (Simoneit, 1988, 1990). The present-day fluids which provide constraints on organic synthesis in submarine hydrothermal systems are those which are free from contamination by sediments. Therefore, it appears that CO_2 is the predominant form of volatile carbon in these fluids, at least at high temperatures.

An explanation why CO_2 and not CH_4 is the dominant form of volatile carbon in present day hydrothermal vent fluids can be found in a consideration of stable thermodynamic equilibrium in the C-H-O system at the oxidation states set by mineral assemblages deep in the oceanic crust and upper mantle where the appropriate fluid/rock reactions occur. As mentioned above, isotopic data indicate that CO_2/CH_4 equilibration only occurs at temperatures > 500°C which indicates that the reaction

$$CO_2 + 4\,H_2 = CH_4 + 2\,H_2O \qquad (12)$$

is reversible only at high temperatures. This observation is consistent with laboratory experiments designed to study this reaction and carbon isotope exchange (see: Shock, 1990b, for a review). Assuming unit activity for H_2O, rearrangement of the logarithmic form of the law of mass action for reaction (12) yields

$$\log fH_2 = \frac{1}{4}\left[\log\left(\frac{fCH_4}{fCO_2}\right) - \log K_{12}\right]. \qquad (13)$$

Values of log K_{12} can be used to evaluate the fugacity ratio of CO_2 to CH_4 consistent with various mineral buffers as shown in Fig. 16 where log fH_2 is plotted against log (fCH_4/fCO_2) at 600°C and 500 bars, conditions where stable equilibrium should prevail. The solid line in Fig. 16 is consistent with Eqn. (13) and log K_{12} = -6.17 at 600 °C and 500 bars (calculated with SUPCRT92). The dashed vertical lines indicate the values of log $f H_2$ set by the mineral buffer assemblages represented by reactions (7-10) at the same temperature and pressure. The points at which the dashed lines intersect the solid line give the fugacity ratios of CH_4 to CO_2 for each buffer assemblage. Note that these values are all less than 1. It follows that CO_2 should be the predominant form of carbon at the high temperatures and pressures encountered deep in hydrothermal systems, and that the high CO_2 to CH_4 ratios in present-day submarine hydrothermal vent fluids are likely to be indicative of high-temperature stable equilibration.

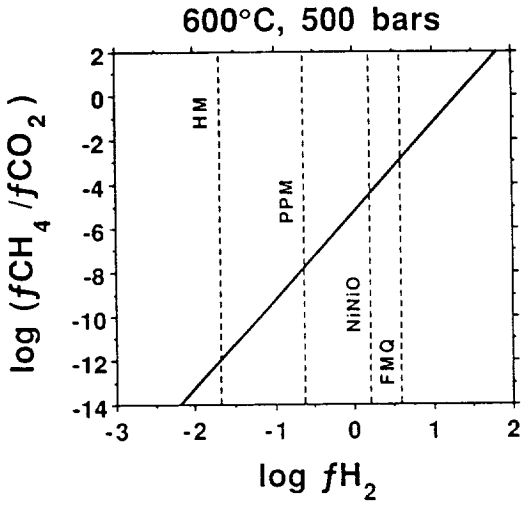

Fig. 16. The ratio of the fugacities of CH_4 and CO_2 as a function of fH_2 at 600°C and 500 bars (solid line). Dashed vertical lines show values of fH_2 buffered by various mineral assemblages (reactions 7 - 10) at the same temperature and pressure.

Calculations of the type shown in Fig. 16 indicate that CO_2 is likely to be the predominant form of volatile carbon presently leaving the Earth's mantle through submarine hydrothermal systems unless the oxidation state of the mantle is considerably more reduced than generally thought (Wood and Virgo, 1989; Bryndzia *et al.*, 1989). These results also suggest that CO_2 would be the predominant product of alteration of carbon-bearing compounds introduced into the high-temperature regions of submarine hydrothermal systems from sources other than the outgassing mantle. Therefore, the extent of

high-temperature hydrothermal alteration of the earliest oceanic crust material and the composition of that crust place constraints on the extent to which organic compounds from accreted meteorites, comets or interplanetary dust particles (Anders, 1989; Chyba *et al.*, 1990; Chyba and Sagan, 1992), or those generated by impacts (Fegley *et al.*, 1986; Fegley and Prinn, 1989; Chyba *et al.*, 1990), would have been altered in early submarine hydrothermal systems. If those systems were generally analogous to present-day systems, then the pervasive high-temperature alteration of oceanic crust near ridge crests would have also altered the accreted carbon-bearing compounds and generated considerable CO_2 (Shock, 1991a). Combined with the rapid annihilation of reduced gases by ultraviolet radiation and hydroxylradical reactions in the atmosphere (Kuhn and Atreya, 1979; Levine *et al.*, 1982; Levine, 1985), high temperature (>500°C) alteration deep in submarine hydrothermal systems may have purged reduced species (such as CH_4, NH_3, HCN, etc.) from the early Earth.

7.2. ORGANIC SYNTHESIS AND BASALT ALTERATION AS COUPLED IRREVERSIBLE PROCESSES

If atmospheric photochemistry and deep-crustal hydrothermal alteration were successful in converting CH_4 and NH_3 to CO_2 and N_2 on the early Earth, then the central dogma of the predominant origin of life theories, chemical evolution from reduced starting materials, is highly doubtful. Under such circumstances, are there environments in which organic synthesis from CO_2 and N_2 can proceed? As mentioned above, these conditions are likely to exist in the upper part of the oceanic crust where hydrothermal systems operate at lower temperatures and at favorable oxidation states set by mineral assemblages. Attainable oxidation states in altered oceanic crust are likely to be spanned by those set by the FMQ and HM buffer assemblages. Is it possible that the same mineral assemblages which would drive the conversion of carbon to CO_2 at stable equilibrium, which would prevail at high temperatures, might also permit organic synthesis at the lower temperatures where metastable states have been shown to persist? The answer to this question is found in calculations similar to those conducted to construct Fig. 16.

Equilibrium constants for reactions (7-10) allow calculation of $\log f\mathrm{H_2}$ values set by the mineral buffer assemblages in altered basalt as functions of temperature and pressure. Values of $f\mathrm{H_2}$ at 500 bars can be compared in Fig. 17. Also shown in Fig. 17 are three contours of $\log (f\mathrm{CO_2}/f\mathrm{CH_4})$ as a function of temperature at 500 bars calculated from the equilibrium constants for reaction (12). These contours are calculated for stable equilibrium, and are plotted here to help delineate conditions where metastable states may exist. As described above, stable equilibrium between CO_2 and CH_4 is unlikely to occur below 500°C in submarine hydrothermal systems. Because organic synthesis requires a departure from stable equilibrium, the dashed vertical line at 500°C indicates an attempt to place an upper temperature boundary on hydrothermal organic synthesis. Note that with decreasing temperature mineral buffers move to lower values of $\log (f\mathrm{CO_2}/f\mathrm{CH_4})$.

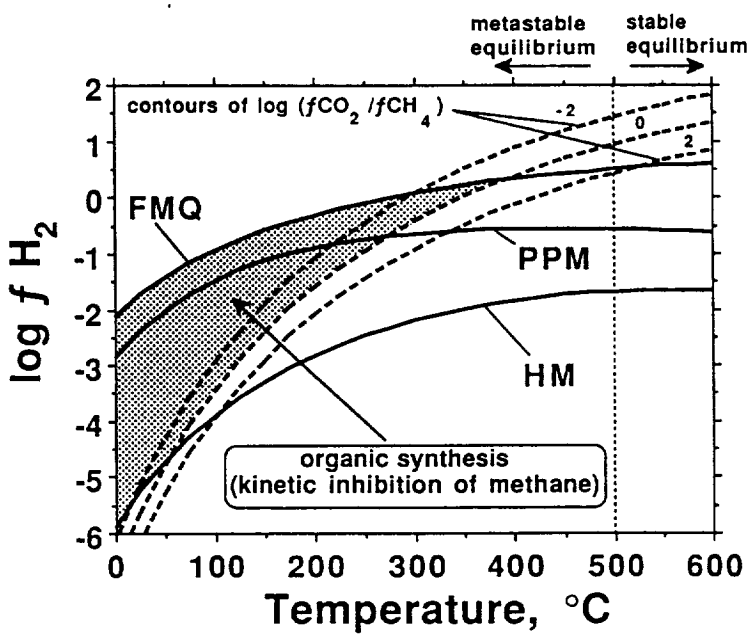

Fig. 17. Plot of log fH_2 against temperature. Solid curves show values of log fH_2 buffered by the FMQ, PPM and HM mineral assemblages as functions of temperature. Dashed curves correspond to contours of log (fCO_2/fCH_4) equal to 2, 0 and -2 as functions of temperature. Dotted vertical line at 500°C separates range of temperature where stable equilibrium in the C-H-O system is attained in submarine hydrothermal systems (T > 500°C), from that at which CO_2 reduction to CH_4 is kinetically inhibited, and where metastable equilibrium states between CO_2 and aqueous organic compounds may prevail. Stippled area corresponds to the region where synthesis of aqueous organic compounds in metastable states may be most easily detected (see text).

Therefore, CO_2 would persist metastably at lower temperatures along a mineral buffer owing to the kinetic inhibition of CH_4 formation. At some point along a mineral-buffered trajectory in Fig. 17, CO_2 would be unstable relative to many organic compounds. Organic synthesis could occur by reduction of CO_2 if such reactions are allowed by reaction kinetics. Although the mechanisms of these reactions are not yet known, the evidence from oil reservoirs cited above indicates that kinetic pathways between CO_2 and organic compounds appear to exist and permit the establishment of metastable equilibrium states in the natural system.

These considerations allow the designation of the field labelled "organic synthesis" in Fig. 17. This field is bounded in log fH_2 by the FMQ and HM curves, which delineate the range of possible fH_2 values owing to the composition of the oceanic crust, and more arbitrarily by the log (fCO_2/fCH_4) = 0 contour. Organic synthesis along a mineral buffer curve in Fig. 17 may begin at lower values of log (fCO_2/fCH_4), but it should be detectable at the zero boundary. With reference to plots of this type, we can follow likely trajectories

taken by fluids as they circulate through the oceanic crust and evaluate whether they encounter the field of possible organic synthesis in hydrothermal systems.

Two schematic fluid circulation paths are shown in the cross section in Fig. 18. Path A follows a trajectory which takes fluids deep into the sheeted dike complex, into the vicinity of the magma chamber and out through ridge-crest black smokers. Path B follows a lower temperature and somewhat shallower trajectory through the flanks of the ridge system. The dotted lines in Fig. 18 indicate isotherms similar to those calculated in many theoretical studies of fluid circulation in the oceanic crust. The numbers along paths A and B indicate specific points along these trajectories where speciation calculations were conducted in the present study. These points are located in $\log f H_2$ vs. temperature space in Fig. 19, and are listed in Table 2. Because temperature and oxidation state are defined for each of these points, we can test the relative effectiveness of these positions in the oceanic crust for organic synthesis from CO_2 and N_2.

General calculations of the type described below are presented for > 80 aqueous organic compounds by Shock (1990b). For the purpose of illustration, and to evaluate the potential of organic synthesis in various regions in the oceanic crust, the calculations described here are for a shortened list of simple organic compounds. The compounds considered in the following calculations are listed in Table 3 and include compounds containing 1 or 2 carbon atoms and/or 1 or 2 nitrogen atoms per molecule. Thermodynamic data and equation-of-state parameters for these aqueous species are taken from Shock et al. (1989), Shock and Helgeson (1990), Shock (1992d), and Schulte and Shock (1992). In the metastable states considered in these calculations, methane, ethane, ethene and ethyne are excluded in order to maintain consistency with evidence from sedimentary basins. In contrast, NH_3 is included in the calculations even though kinetic barriers to its formation from N_2 may exist. Insufficient analytical data from natural systems precludes a quantitative assessment of this possibility. Therefore, without the necessary data to exclude NH_3, the decision was made to include it. If a kinetic barrier to NH_3 formation exists, then calculated activities of N-bearing organic compounds would be higher than those obtained in this study. All of the calculations conducted in this study are for 500 bars total pressure, initial fugacities of CO_2 and N_2 equal to 10 bars and 1 bar, respectively, and unit activity of H_2O. These high values for CO_2 and N_2 are used to simulate either a rapid outgassing of the mantle or efficient cycling of volatiles from comets and/or meteorites through the deepest portions of the oceanic crust.

Calculation of the distribution of species in the metastable states described above requires mass-action and mass-balance constraints. Mass-action constraints for the fourteen product compounds listed in Table 3 are given by the equilibrium constants for reactions of the type

$$a\,CO_2 + b\,N_2 + c\,H_2 = d\,\text{product} + e\,H_2O \qquad (14)$$

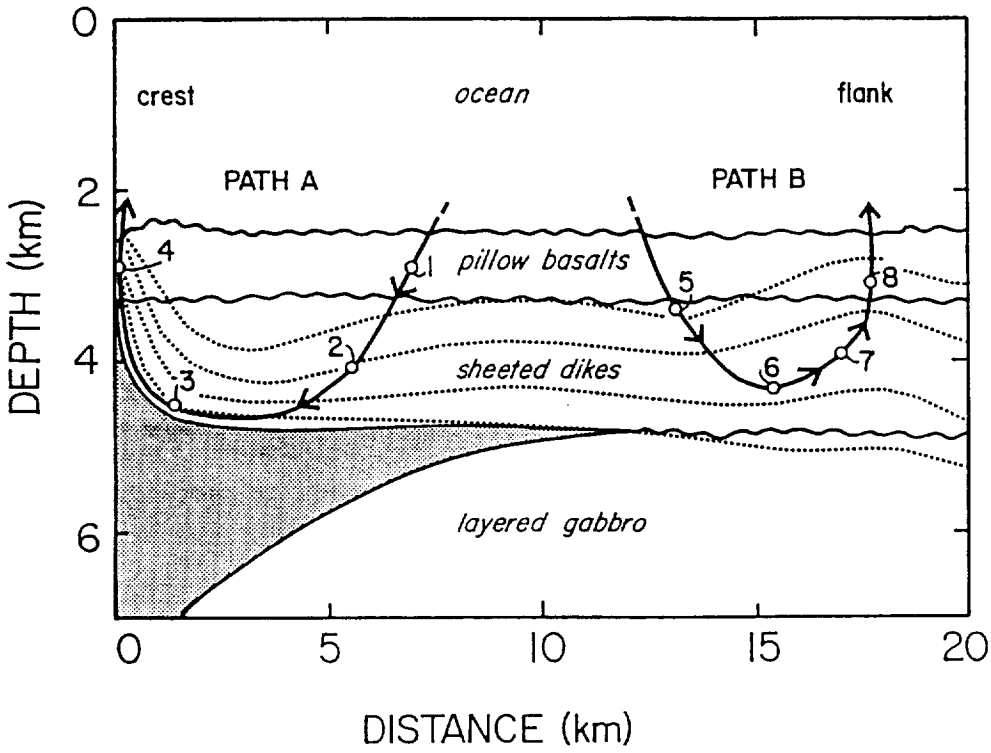

Fig. 18. Schematic cross section of oceanic crust at a spreading center showing two possible flow paths for hydrothermal fluids. Dotted curves represent isotherms consistent with the model of Fehn *et al.* (1983). Path A follows fluids from a seawater recharge zone to depths in excess of 4 km in oceanic crust where they are heated near the magma chamber before exiting at the ridge-crest in black smoker vents. Path B follows fluids from a seawater recharge zone through the flanks of the ridge system. Estimates of fluid flow through the oceanic crust indicate that flow through paths like B exceeds the flow through paths like A by more than a factor of 20. The stippled area indicates a magma chamber consisting of liquid and crystal-mush regions. Locations numbered 1-8 correspond to points along the flow paths which are likely to be characterized by the temperature and mineral assemblages listed in Table 2, and are used for reference in Figs. 19-24.

where a-e represent stoichiometric reaction coefficients. The set of equilibrium constants differs at each temperature considered. Fourteen reactions of the type given by reaction (14) are combined with four mass-balance constraints for C, N, H and O to construct a matrix of eighteen equations solved simultaneously. One example of the mass-balance constraints is that all of the carbon redistributed into products, as well as that remaining as CO_2, must sum to equal the initial 10 bars of CO_2. Results of these calculations at points 1-8 defined in Table 2 are listed in Table 4. This set of results is depicted in various sub-groupings in Figs. 20-24.

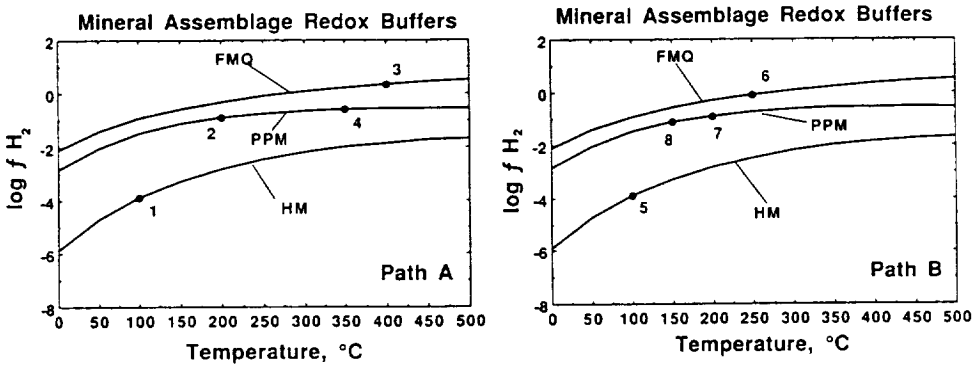

Fig. 19. Plots of log fH_2 against temperature (in °C) showing locations of points on the flow paths in Fig. 18 and listed in Table 2.

TABLE 2

Temperatures and fH_2 buffer assemblages at points along paths A and B in Fig. 18

Point	Temperature, °C	fH_2 buffer
1	100	HM
2	200	PPM
3	400	FMQ
4	350	PPM
5	100	HM
6	250	FMQ
7	200	PPM
8	150	PPM

TABLE 3

Species involved in the distribution of species calculations depicted in Figs. 20-24

Reactants:	
CO_2, N_2, H_2, H_2O	
Products:	
CO, NH_3, HCN,	
formaldehyde	H_2CO
acetaldehyde	CH_3HCO
methanol	CH_3OH
ethanol	C_2H_5OH
formic acid	HCOOH
acetic acid	CH_3COOH
methanamine	CH_3NH_2
ethanamine	$C_2H_5NH_2$
urea	$CO(NH_2)_2$
oxalic acid	$(COOH)_2$
glycine	$C_2H_5NO_2$

Results from Table 4 for the fourteen aqueous organic species which are reaction products in the metastable equilibrium state examined by the distribution of species calculations are shown in the following groupings: compounds with one carbon atom in Fig. 20, compounds with two carbon atoms in Fig. 21, compounds with one oxygen atom in Fig. 22, compounds containing nitrogen in Fig. 23, and organic acids in Fig. 24. These groupings allow many species to be represented more than once which facilitates comparisons among the results. A general trend can be observed on each pair of figures showing results along paths A and B. In each case, the calculated activities of aqueous organic species are higher at the final point along path B than at the end of path A. This indicates that organic synthesis in submarine hydrothermal systems is more likely in fluids circulating through the flanks rather than those circulating through the ridge-crust and venting at black smokers (see Fig. 18), a point made previously by Shock (1990b, 1991b).

TABLE 4

Log activities of aqueous species from speciation calculations for points along paths A and B in Fig. 18 using temperatures and fH_2 values consistent with mineral buffers as listed in Table 2, and initial fugacities of CO_2 and N_2 set to 10 bars and 1 bar, respectively

Products	#1 (also #5)	#2 (also#7)	#3	#4	#6	#8
CO	-10.00	-6.56	-3.55	-5.05	-5.41	-7.05
NH_3	-4.19	-1.99	-2.50	-3.47	-1.58	-1.33
HCN	-18.69	-12.74	-10.58	-12.82	-11.15	-12.68
formaldehyde	-14.25	-9.02	-6.84	-8.78	-7.63	-9.15
acetaldehyde	-16.50	-8.84	-9.71	-13.19	-7.29	-6.78
methanol	-12.55	-7.18	-6.79	-9.04	-5.96	-6.29
ethanol	-16.25	-7.93	-9.92	-13.87	-6.36	-5.09
formic acid	-8.11	-5.91	-5.09	-6.07	-5.35	-5.80
acetic acid	-9.22	-4.66	-7.11	-9.56	-3.99	-2.33
methanamine	-15.32	-8.59	-9.77	-12.77	-7.28	-6.67
ethanamine	-20.56	-10.65	-14.04	-18.76	-8.93	-6.88
urea	-10.37	-7.46	-10.08	-11.78	-7.19	-5.47
oxalic acid	-17.79	-15.49	-14.66	-15.63	-14.91	-15.41
glycine	-16.78	-12.12	-16.15	-18.56	-11.65	-9.24

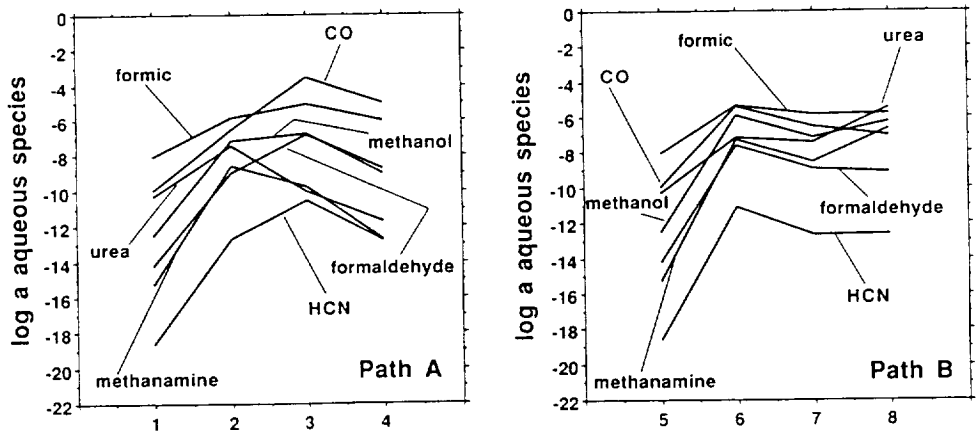

Fig. 20. Plots of log activity of aqueous species containing one atom of carbon per molecule taken from Table 4 as functions of the points along the flow paths indicated in Figs. 18 and 19 and Table 2.

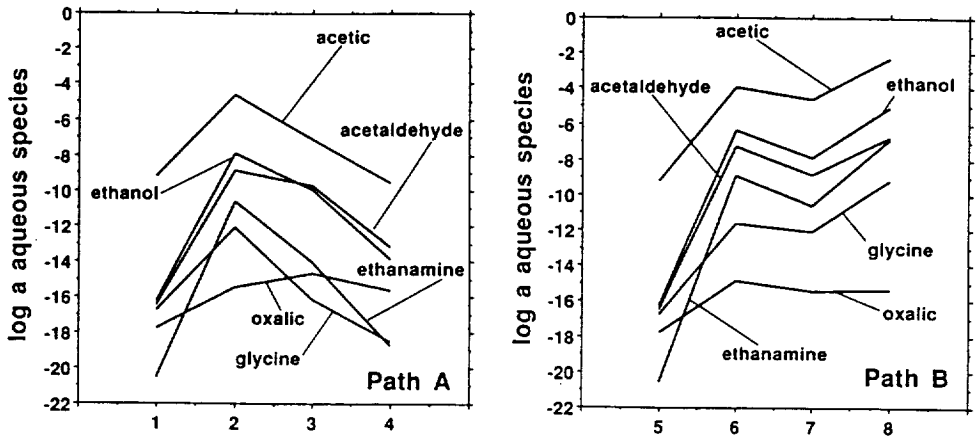

Fig. 21. Plots of the log activity of aqueous species containing two carbon atoms per molecule taken from Table 4 as functions of the points along the flow paths indicted in Figs. 18 and 19 and Table 2.

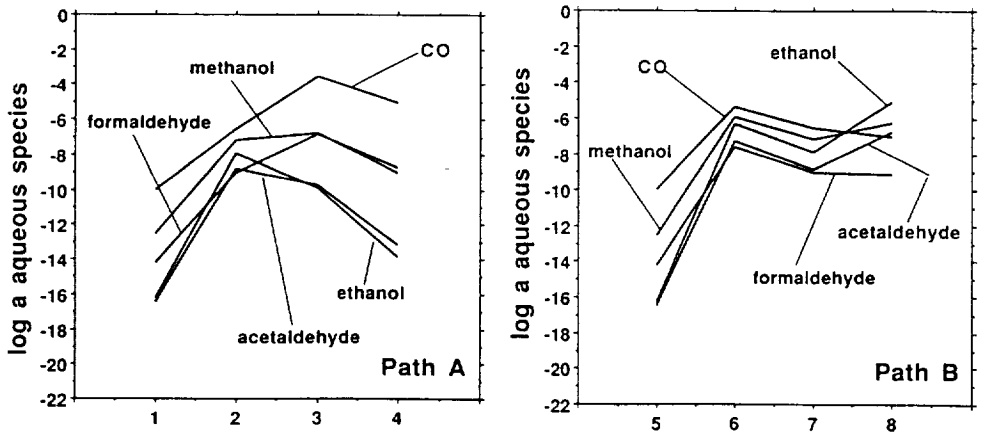

Fig. 22. Plots of the log activity of aqueous species containing one oxygen atom per molecule taken from Table 4 as functions of the points along the flow paths indicted in Figs. 18 and 19 and Table 2.

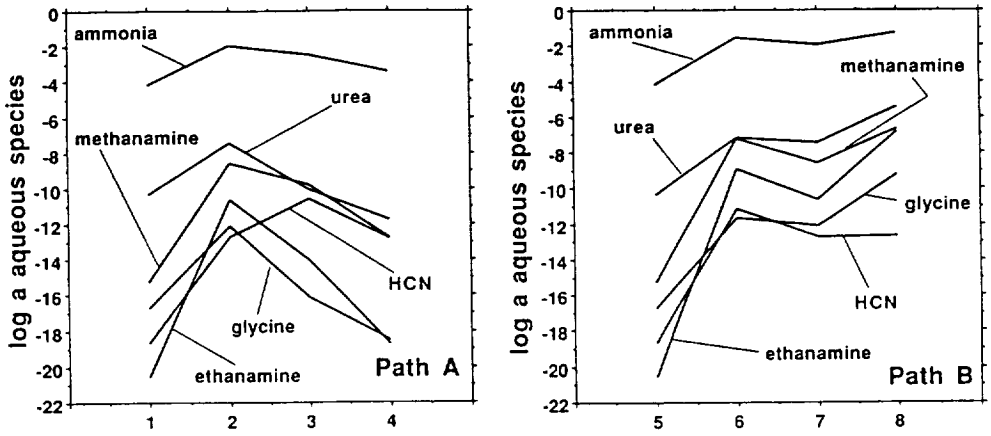

Fig. 23. Plots of the log activity of aqueous species containing nitrogen taken from Table 4 as functions of the points along the flow paths indicted in Figs. 18 and 19 and Table 2.

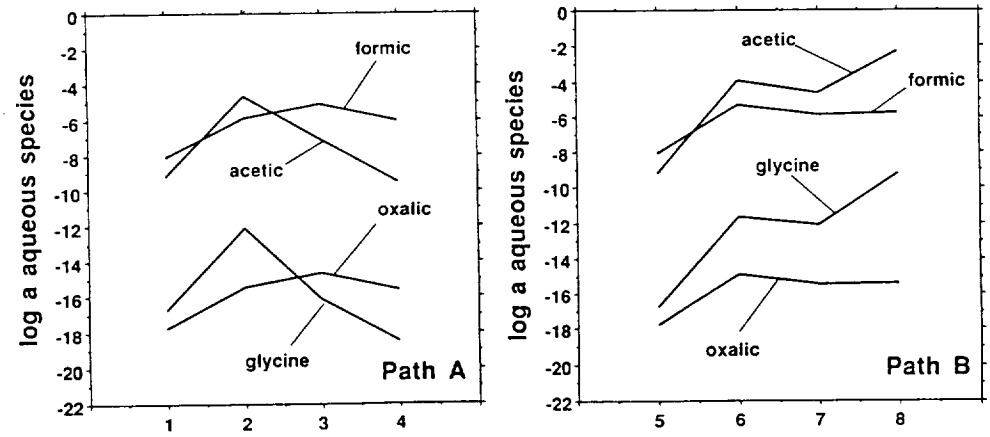

Fig. 24. Plots of the log activity of aqueous organic acids taken from Table 4 as functions of the points along the flow paths indicted in Figs. 18 and 19 and Table 2.

Specific comparisons of the results in Figs. 20-24 may help to focus experimental investigations on the most likely environments in submarine hydrothermal systems for organic synthesis. Comparison of Figs. 20A and B shows that CO is the predominant 1-carbon species at points 3 and 4 along path A, and second only to formic acid at points 1 and 2. In contrast, the activity of CO is lower than those of urea, formic acid, methanol and methanamine at the final point along path B. For the sake of comparison, let us consider activities = 10^{-8} as a threshold above which the activities of aqueous species become significant in the speciation of hydrothermal fluids. Along path A, CO, formic acid, methanol, urea and formaldehyde cross this threshold as shown in Fig. 20A. At point 4, which represents the possible final metastable equilibration before venting at black smokers, only CO and formic acid are across this threshold. In contrast, calculated activities of all of the 1-carbon species except HCN cross this 10^{-8} threshold along path B as shown in Fig. 20B, and all but HCN and formaldehyde are present at activities > 10^{-8} at point 8, a possible final metastable equilibrium state achieved before venting.

Differences between paths A and B are more dramatic for the 2-carbon species shown in Figs. 21A and B. Note that acetic acid is the only 2-carbon species to cross the 10^{-8} threshold at points along path A (Fig. 21A), but that acetic acid, ethanol, acetaldehyde and ethanamine cross this threshold at points along path B (Fig. 21B). Comparison of points 4 and 8 shows that no 2-carbon species have calculated activities > 10^{-8} at black smoker conditions, but that four 2-carbon species have activities > 10^{-8} in calculations appropriate for flank hot spring environments. Note that among these aqueous organic species, the calculated activity of acetic acid approaches 10^{-2} at point 8 along path B. As a comparison, activities of acetic acid in sedimentary basin brines are in the range 10^{-4} to 10^{-2} (Shock 1988, 1989, 1990c).

Among the 1-oxygen compounds shown in Figs. 22A and B, CO is predominant at all points along all of path A and most of path B. Calculated activities of methanol, formaldehyde and CO cross the 10^{-8} threshold along path A, but only CO remains at point 4. In contrast, calculated activities of all of the 1-oxygen species cross this threshold along path B, and all but formaldehyde remain at point 8. Note that the calculated activities of ethanol, methanol and acetaldehyde exceed that of CO at point 8 and that the calculated activity of ethanol approaches 10^{-5}. As in the cases of the 1- and 2-carbon species shown in Figs. 20 and 21, the results shown in Fig. 22 suggest that fluids circulating through the flanks of ridge systems have the greater potential for organic synthesis.

The calculated activities of nitrogen-bearing species shown in Fig. 23 are also consistent with the hypothesis that flank environments may be more suitable for organic synthesis than crest environments. Comparison of Figs. 23A and B shows that ammonia is the predominant product at all points along both paths. Along path A, the calculated activity of urea crosses the 10^{-8} threshold at point 2 but plunges well below this value, like the other N-bearing organic compounds, at points 3 and 4. In contrast, urea, methanamine and ethanamine have calculated activities which exceed 10^{-8} at points along path B. Note that all of the calculated activities of N-bearing organic compounds increase along path B,

and that the calculated activity of urea is ~ $10^{-5.5}$ at point 8. In contrast, the calculated activities of N-bearing organic compounds increase from point 1 to point 2 along path A, corresponding to downward flow of hydrothermal fluids near ridge crests, but decrease dramatically along the upward flow path to the black smokers as represented by points 3 and 4. As mentioned above, kinetic barriers to the formation of NH_3 from N_2 at low temperatures would allow greater calculated activities of N-bearing aqueous organic compounds.

The results shown in Figs. 24A and B are also shown in the other figures, but are isolated in this figure in order to compare results for the organic acids considered in these calculations. Results for formic and oxalic acids are remarkably similar along paths A and B as shown in Fig. 24. In contrast, those for acetic acid and glycine differ dramatically between the two paths. Along path A, the calculated activity of formic acid is generally greater that for acetic acid. However, the opposite is the case along path B. The predominance of acetic acid over formic acid along path B resembles the relative abundances in sedimentary basin brines in which acetic acid is abundant and formic acid is seldom detected (Carothers and Kharaka, 1978). In addition, the calculated activity of glycine, which decreases to nearly 10^{-19} at point 4 along path A, increases by eight orders of magnitude along path B and approaches 10^{-9} at point 8. These results, together with those summarized in Figs. 20-23, as well as those presented by Shock (1990b), can be used to identify environments in submarine hydrothermal systems where organic synthesis may be favorable. They also serve as predictions which can be used to guide experimental studies. In addition, these results can be used to estimate the possible contributions of submarine hydrothermal synthesis as the budget of organic carbon on the early Earth.

7.3. SUBMARINE HYDROTHERMAL SYSTEMS AS SOURCES OF ORGANIC COMPOUNDS

The results summarized above indicate that calculated activities of aqueous organic compounds in metastable equilibrium states are greater along flow paths through the flanks of mid-ocean ridge systems than they are along flow paths through the ridge crest which exit the oceanic crust at black-smoker vents. For example, the calculated activity of acetic acid along path B reaches $10^{-2.33}$. It should be kept in mind that the calculations described above are for an initial CO_2 fugacity of 10 bars which may be high, and that the corresponding activities of aqueous organic species may represent maximum values. Therefore, if we take 10^{-5} as an attainable activity of acetic acid at ~200°C in ridge-flank fluids, we can place some constraints on the carbon-fixing potential of submarine hydrothermal systems.

The molecular weight of acetic acid is 60.053 g mol^{-1}, and assuming that molalities and activities are equivalent for highly dilute species in hydrothermal fluids the corresponding concentration of acetic acid would be 6 x 10^{-4} g kg^{-1} or 0.6 ppm by weight.

Acetic acid is ~40% (by weight) carbon, so the corresponding concentration of organic carbon would be 0.24 ppm. As described above, estimates of fluid flux through present-day ridge-flank hydrothermal systems yield 10^{14} to 10^{15} kg yr^{-1}. Therefore the potential organic carbon productivity of submarine hydrothermal systems would be ~2 x 10^{7} to 2 x 10^{8} kg yr^{-1} at present. Fluid flow and the potential for organic synthesis may have been considerably greater on the early Earth which was probably considerably warmer with higher heat flow and more rapid seafloor spreading rates.

TABLE 5
Comparison of various potential sources of organic compounds on the early Earth

Source[a]	Organic production reduced atmosphere (kg yr^{-1})	Organic production neutral atmosphere (kg yr^{-1})
Lightning	3 x 10^{9}	3 x 10^{7}
Coronal discharge	2 x 10^{8}	2 x 10^{6}
Ultraviolet light[b]	2 x 10^{11}	3 x 10^{8}
Atmospheric shocks from meteors	1 x 10^{9}	3 x 10^{1}
Atmospheric shocks from post-impact plumes	2 x 10^{10}	4 x 10^{2}
Interplanetary dust particles	6 x 10^{7}	6 x 10^{7}
Hydrothermal synthesis	2 x 10^{8}	2 x 10^{8}

[a] values for all sources other than hydrothermal synthesis are taken from Chyba and Sagan (1992).

[b] values for ultraviolet light represent the sum of productivity from various wavelengths (see Chyba and Sagan, 1992).

Part of the organic production in the flank systems would be offset by destruction in ridge-crest hydrothermal systems as advocated by Miller and Bada (1988, 1991a,b), and consistent with results described above. However, the destructive flow through the ridge-crests is estimated to be 5% of the productive flow through the flanks (COSOD II, 1987, see above). It follows that destruction of aqueous organic species at ridge-crests is nearly insignificant and has only the slightest impact on the potential of submarine hydrothermal systems for organic synthesis. Given the potential for greater productivity on a warmer early Earth than at present, 2×10^8 kg yr^{-1} is likely to be a reasonable estimate of the potential productivity of hydrothermal systems.

To place hydrothermal organic synthesis in perspective, comparisons should be made of the rates of organic productivity obtained above with those from other sources both terrestrial and extraterrestrial. Chyba and Sagan (1992) provide a summary of their best estimates of various sources of organic compounds on the early Earth other than hydrothermal systems. Rates of organic production form Chyba and Sagan (1992) are listed in Table 5, together with that obtained in this study for hydrothermal synthesis. Chyba and Sagan (1992) perform calculations for a reduced atmosphere rich in CH_4 with H_2O and either N_2 or NH_3, and a neutral atmosphere rich in CO_2, with H_2O and N_2. For reasons described above, the results for the reduced atmosphere are unlikely to be applicable to the early Earth. Comparison of hydrothermal synthesis and all other sources can be made with the values in the right-hand column of Table 5. The sum of organic contributions and production from all sources other than hydrothermal synthesis is $\sim 4 \times 10^8$ kg yr^{-1} for a neutral atmosphere. This value is only a factor of two greater than the potential contribution from hydrothermal synthesis as evaluated in the present study. This suggests that hydrothermal synthesis of organic compounds should receive considerable experimental and theoretical attention in order for progress to be made in the study of the origin of life.

Acknowledgements

The research described above benefitted from discussions with Dimitri Sverjensky, Mitch Schulte, Harold Helgeson, Dave Sassani, Nils Holm, Bruce Fegley, Sherwood Chang, Mike Engel, Bernd Simoneit, Steve Macko and Tom McCollom. Technical assistance from Carla Koretsky, Patty DuBois and Allison Shock is greatly appreciated, as are reviews from John Kerridge and Sherwood Chang. This work was funded in part by NSF grant EAR-9018468 and NASA grant NAGW-2818.